

NLO QCD corrections to $t\bar{t}b\bar{b}$ production at the LHC: 2. full hadronic results

A. BREDENSTEIN¹, A. DENNER², S. DITTMAYER³ AND S. POZZORINI⁴

¹ *High Energy Accelerator Research Organization (KEK),
Tsukuba, Ibaraki 305-0801, Japan*

² *Paul Scherrer Institut, Würenlingen und Villigen,
CH-5232 Villigen PSI, Switzerland*

³ *Albert-Ludwigs-Universität Freiburg, Physikalisches Institut,
D-79104 Freiburg, Germany*

⁴ *Physics Department, Theory Group, CERN,
CH-1211 Geneva 23, Switzerland*

Abstract:

We present predictions for $t\bar{t}b\bar{b}$ production at the LHC in next-to-leading order QCD. The precise description of this background process is a prerequisite to observe associated $t\bar{t}H$ production in the $H \rightarrow b\bar{b}$ decay channel and to directly measure the top-quark Yukawa coupling at the LHC. The leading-order cross section is extremely sensitive to scale variations. We observe that the traditional scale choice adopted in ATLAS simulations underestimates the $t\bar{t}b\bar{b}$ background by a factor two and introduce a new dynamical scale that stabilizes the perturbative predictions. We study various kinematic distributions and observe that the corrections have little impact on their shapes if standard cuts are applied. In the regime of highly boosted Higgs bosons, which offers better perspectives to observe the $t\bar{t}H$ signal, we find significant distortions of the kinematic distributions. The one-loop amplitudes are computed using process-independent algebraic manipulations of Feynman diagrams and numerical tensor reduction. We find that this approach provides very high numerical stability and CPU efficiency.

1 Introduction

The discovery of the Higgs boson and the measurement of its interactions with massive quarks and vector bosons represent a central goal of the ATLAS [1,2] and CMS [3] experiments at the Large Hadron Collider (LHC). The present limits from direct searches and electroweak precision measurements favour a Higgs-mass range below the W -decay threshold. In this light-Higgs scenario, the Higgs predominantly decays into bottom quarks, and its observation is very challenging at the LHC. In the dominant Higgs-production channel, i.e. in gluon-gluon fusion, the $H \rightarrow b\bar{b}$ signal is completely obscured by a huge QCD background.

Associated production mechanisms, where the Higgs boson is accompanied by a massive gauge boson or top-quark pairs, feature more distinctive signatures that can be exploited to reduce the background to the $H \rightarrow b\bar{b}$ final state. These associated Higgs-production channels provide direct access to the interactions of the Higgs boson with gauge bosons and heavy quarks. Their observation would permit to test the electroweak symmetry-breaking mechanism. But the QCD background to associated WH , ZH , and $t\bar{t}H$ production followed by $H \rightarrow b\bar{b}$ decay remains a critical issue, which requires significant progress in two directions. The low signal-to-background ratios must be increased by means of improved selection strategies; and more precise descriptions of the background are needed in order to reduce systematic uncertainties. In this paper we address the latter issue by providing next-to-leading-order (NLO) QCD predictions for the irreducible QCD background to $t\bar{t}H(H \rightarrow b\bar{b})$ production.

The strategies elaborated by ATLAS and CMS to identify the $t\bar{t}H(H \rightarrow b\bar{b})$ signal [2–7] are based on the full reconstruction of the $t\bar{t}b\bar{b}$ signature, starting from a final state with four b quarks and additional light jets. After imposing four b -taggings, a reconstruction of the top quarks is performed. This permits to identify two b quarks as top-decay products. The remaining two b quarks constitute a Higgs candidate, and their invariant-mass distribution is the relevant observable to find the Higgs signal. However, the presence of multiple b quarks and light jets in the final state represents a serious obstacle to the correct identification of the $b\bar{b}$ Higgs candidates. Realistic simulations indicate that only about 1/3 of the selected b -quark pairs have correct combinatorics, while the other Higgs candidates contain b jets from top decays or miss-tagged light jets. This so-called combinatorial background significantly dilutes the Higgs signal and increases its background contamination. The QCD processes $pp \rightarrow t\bar{t}b\bar{b}$ and $t\bar{t}jj$ are the main background components. The latest ATLAS and CMS simulations [2, 3], for 30 fb^{-1} and 60 fb^{-1} , respectively, anticipate a statistical significance around 2σ (ignoring systematic uncertainties) and a fairly low signal-to-background ratio of order 1/10. This calls for better than 10% precision in the background description, a very demanding requirement both from the experimental and theoretical point of view.

More recently, alternative search strategies based on the selection of highly boosted Higgs bosons, which decay into “fat jets” containing two b quarks, have opened new and very promising perspectives, both for $VH(H \rightarrow b\bar{b})$ [8] and $t\bar{t}H(H \rightarrow b\bar{b})$ [9]. In the case of $t\bar{t}H$, this novel approach might enable a better background suppression and increase the signal-to-background ratio beyond 1/3. Moreover, three b -taggings would be

sufficient to strongly suppress the $t\bar{t}jj$ contamination. In this case the background would be completely dominated by $t\bar{t}b\bar{b}$ production.

The calculation of the NLO QCD corrections to the process $pp \rightarrow t\bar{t}b\bar{b}$, first presented in Refs. [10,11] and subsequently confirmed in Ref. [12], constitutes another important step towards the observability of the $t\bar{t}H(H \rightarrow b\bar{b})$ signal at the LHC. The ATLAS simulations of the $t\bar{t}b\bar{b}$ background [2,4,5] are based on leading-order (LO) matrix elements and the scale choice $\mu_R = \mu_F = E_{\text{thr}}/2$, where $E_{\text{thr}} = 2m_t + m_{b\bar{b}}$ is the partonic threshold energy.¹ These predictions suffer from huge scale uncertainties: the LO $t\bar{t}b\bar{b}$ cross section can vary up to a factor four if the renormalization and factorization scales are identified with different kinematic parameters [4]. However, in the case of the $t\bar{t}H$ signal [13,14] it was found that setting the QCD scale equal to half the threshold energy leads to fairly moderate NLO corrections ($K \simeq 1.2$). The same behaviour was subsequently observed in two other processes that feature a final state similar to $t\bar{t}b\bar{b}$. At the scale $\mu_{R,F} = E_{\text{thr}}/2$, the NLO QCD corrections to $pp \rightarrow t\bar{t}j$ [15] and $t\bar{t}Z$ [16] at the LHC amount to $K \simeq 1.0\text{--}1.15$ (for $p_{T,\text{jet}} \gtrsim 20\text{--}50$ GeV) and $K \simeq 1.35$, respectively. On the basis of these observations one might have expected that LO $t\bar{t}b\bar{b}$ predictions obtained with the same scale choice might have a decent level of precision, say at the 20–30% level. However, it turned out that the NLO corrections to $t\bar{t}b\bar{b}$ production, for $\mu_{R,F} = E_{\text{thr}}/2$, are much larger and correspond to a K factor of about 1.8 [11,12]. Apart from the sizable impact on the $t\bar{t}H$ analysis, this big K factor suggests the presence of large logarithms that tend to spoil the convergence of the perturbative expansion. As we argue, this is mainly due to the fact that the scale $\mu_{R,F} = E_{\text{thr}}/2$ does not provide an adequate description of the QCD dynamics of $t\bar{t}b\bar{b}$ production. To cure this problem we introduce a new and more natural scale choice. This leads to a much smaller K factor and also reduces the residual scale dependence at NLO. Besides the issue of scale dependences, in this paper we also investigate NLO effects on various differential distributions and selection cuts that are relevant for the $t\bar{t}H$ analysis, both within the traditional ATLAS/CMS approach and in the boosted-Higgs framework.

In addition to its phenomenological relevance, the calculation of the NLO corrections to $pp \rightarrow t\bar{t}b\bar{b}$ constitutes also an important technical benchmark. The description of many-particle processes at NLO plays an important role for the LHC physics programme [17,18]. Numerous Higgs and new-physics signals, as well as their background, are characterized by multi-particle final states. These processes often involve high powers of α_s that give rise to very large scale uncertainties if NLO effects are not taken into account. The most prominent multi-particle reactions that require NLO predictions are summarised in the so-called Les Houches priority list [17,18]. In the recent years, the technical challenges raised by these calculations have triggered an impressive amount of conceptual and technical developments. In particular, in order to treat one-loop amplitudes with particle multiplicities higher than five, various methods based on tensor integrals [19–28] or on-shell reductions [29–44] have been developed. Very recently, these different techniques have lead to the first NLO results for six-particle processes at the LHC, namely for $pp \rightarrow t\bar{t}b\bar{b}$ [11,12], the leading- [45] and the full-colour contributions [46] to $pp \rightarrow Wjjj$, and for the $q\bar{q}$ contribution to $pp \rightarrow b\bar{b}b\bar{b}$ [47].

¹The scale choice adopted in the CMS simulations [3,6,7] is not documented.

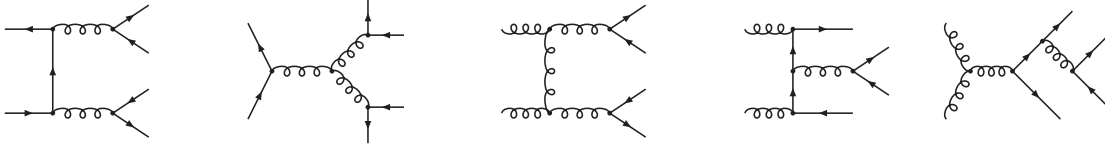


Figure 1: Sample tree diagrams contributing to the $q\bar{q} \rightarrow t\bar{t}b\bar{b}$ and $gg \rightarrow t\bar{t}b\bar{b}$ channels.

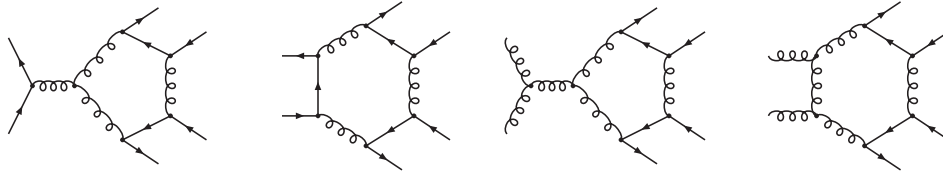


Figure 2: Sample pentagon and hexagon graphs contributing to $q\bar{q} \rightarrow t\bar{t}b\bar{b}$ and $gg \rightarrow t\bar{t}b\bar{b}$. The gg ($q\bar{q}$) channel comprises in total 1003 (188) graphs, including 40 (8) hexagons and 114 (24) pentagons.

To compute the virtual corrections to $t\bar{t}b\bar{b}$ production we employ explicit diagrammatic representations of the one-loop amplitudes. A key feature of our approach is the factorization of colour structures at the level of individual diagrams. This permits to reduce the CPU cost of colour sums essentially to zero. Helicity-dependent structures are algebraically reduced to a common set of so-called standard matrix elements. In this way the sums over physical helicities are strongly boosted. Tensor loop integrals are related to scalar integrals by means of numerical algorithms that systematically avoid numerical instabilities from inverse Gram determinants and other spurious singularities [20, 21]. The efficiency of the calculation is strongly increased by recycling a multitude of common subexpressions, which occur both inside individual diagrams and in tensor integrals of different diagrams that share common sub-topologies. As demonstrated by the remarkably high CPU speed of the numerical code, these procedures strongly mitigate the factorial complexity that is inherent in Feynman diagrams. The real corrections are handled with the dipole subtraction method [50–53], and the phase-space integration is performed with adaptive multi-channel methods [54–56]. Our results have been confirmed with the OPP method [41–44] and HELAC-1LOOP [48, 49] within the statistical Monte Carlo error of 0.2% [12].

The paper is organised as follows. Section 2 is devoted to technical aspects of the calculation of the virtual and real corrections. In Section 3 we present predictions for the LHC. In particular, we discuss the scale dependence and investigate NLO effects on the shape of several distributions. Our results are summarised in Section 4. In App. A we outline the algebraic reduction of helicity structures, and in App. B we provide benchmark results for the matrix element squared in lowest order and including virtual corrections for one phase-space point.

2 Details of the calculation

In LO, the hadronic production of $t\bar{t}b\bar{b}$ proceeds via the partonic processes $q\bar{q} \rightarrow t\bar{t}b\bar{b}$ and $gg \rightarrow t\bar{t}b\bar{b}$, which are described by 7 and 36 tree diagrams, respectively (see Figure 1). The virtual NLO QCD corrections to these channels involve 188 and 1003 one-loop di-

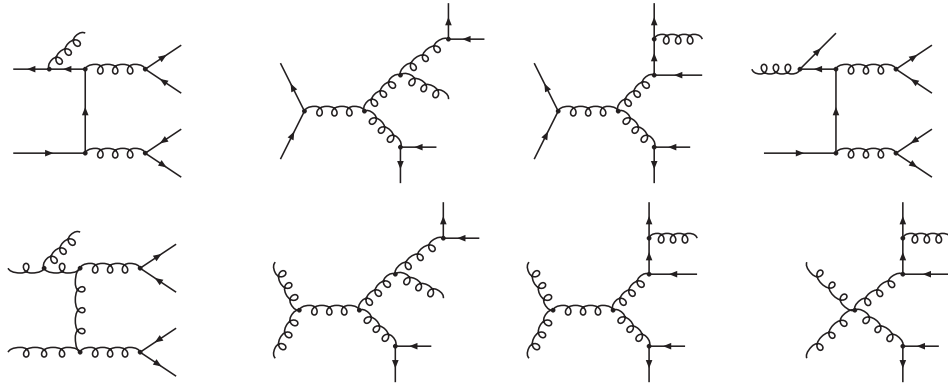


Figure 3: Sample real-emission diagrams contributing to the channels $q\bar{q} \rightarrow t\bar{t}b\bar{b}g$, $qg \rightarrow t\bar{t}b\bar{b}q$, and $gg \rightarrow t\bar{t}b\bar{b}g$.

agrams, respectively. A few examples of pentagon and hexagon graphs are illustrated in Figure 2. The real emission contributions are induced by the partonic processes $q\bar{q} \rightarrow t\bar{t}b\bar{b}g$, $gg \rightarrow t\bar{t}b\bar{b}g$, $qg \rightarrow t\bar{t}b\bar{b}q$, and $g\bar{q} \rightarrow t\bar{t}b\bar{b}q$. The gg channel involves 341 tree diagrams. The $q\bar{q}$, qg and $g\bar{q}$ channels, which are related by crossing transformations, are described by 64 tree diagrams each (see Figure 3).

In the following we describe the calculation of the virtual and real NLO corrections. Each of these contributions has been worked out twice and independently, resulting in two completely independent computer codes. Top quarks are treated fully inclusively, i.e. we do not include top decays. Moreover we handle bottom quarks in the massless approximation, corresponding to the five-flavour scheme. However, we do not take into account the suppressed contribution from initial-state bottom quarks.

2.1 Virtual corrections

The virtual corrections are generated with two in-house MATHEMATICA programs that reduce Feynman diagrams and generate FORTRAN77 code in a fully automatized way. One of the two programs relies on FORMCALC 5.2 [57] for preliminary algebraic manipulations. Here we outline the underlying structure of the calculation, with emphasis on colour/helicity structures and tensor integrals. In this respect, both programs are organised in a fairly similar way. Since the treatment of the $q\bar{q}$ channel is already documented in Ref. [10], we focus on the gg channel.

Diagram-by-diagram approach

The virtual corrections are obtained from the interference of the one-loop and LO matrix elements summed over external-state colours and helicities. This quantity is computed on a diagram-by-diagram basis,

$$\sum_{\text{col}} \sum_{\text{hel}} \mathcal{M}^{(1\text{-loop})} (\mathcal{M}^{(\text{LO})})^* = \sum_{\Gamma} \left[\sum_{\text{col}} \sum_{\text{hel}} \mathcal{M}^{(\Gamma)} (\mathcal{M}^{(\text{LO})})^* \right]. \quad (2.1)$$

The contributions of individual loop diagrams (Γ) are evaluated by separate numerical routines and summed explicitly. The Feynman diagrams are generated with two independent tools, FEYNARTS 1.0 [58] and FEYNARTS 3.2 [59].

Colour factorization

One of the key features of the diagram-by-diagram approach is that the cost related to the large number of diagrams is compensated by the possibility to perform colour sums very efficiently. This is a consequence of colour factorization: individual (sub)diagrams consist of a single colour-stripped amplitude $\mathcal{A}^{(\Gamma)}$ multiplied by a trivial colour factor $\mathcal{C}^{(\Gamma)}$,

$$\mathcal{M}^{(\Gamma)} = \mathcal{A}^{(\Gamma)}\mathcal{C}^{(\Gamma)}. \quad (2.2)$$

More precisely, each diagram gives rise to 3^{n_4} colour-factorized contributions of type (2.2), where n_4 is the number of quartic gluon vertices in the diagram. These terms are handled as separate subdiagrams. However, most diagrams do not involve quartic couplings, and their colour structures factorize completely. For instance, the last diagram in Figure 2 involves a single colour structure

$$\mathcal{C}^{(\text{hex})} = \sum_{b,c,d,e} f^{a_1bc} f^{a_2cd} (T^b T^e)_{i_3 i_4} (T^d T^e)_{i_5 i_6}, \quad (2.3)$$

where a_1, a_2 and i_3, i_4, i_5, i_6 are the colour indices of the gg and $t\bar{t}b\bar{b}$ external states, numbered in this order. All colour structures can be easily reduced to Kronecker symbols and Gell-Mann matrices $T^a = \lambda^a/2$ by using

$$f^{abc}T^c = -i[T^a, T^b], \quad T_{ij}^a T_{kl}^a = \frac{1}{2} \left(\delta_{il}\delta_{kj} - \frac{1}{N_c} \delta_{ij}\delta_{kl} \right), \quad (2.4)$$

and other well-known $SU(N_c)$ relations. In the gg channel, this reduction leads to a colour basis of 14 elements,

$$\begin{aligned} \mathcal{C}_1 &= T_{i_3 i_4}^{a_1} T_{i_5 i_6}^{a_2}, & \mathcal{C}_2 &= \delta_{i_3 i_4} (T^{a_1} T^{a_2})_{i_5 i_6}, & \mathcal{C}_3 &= \delta_{i_3 i_4} (T^{a_2} T^{a_1})_{i_5 i_6}, \\ \mathcal{C}_4 &= T_{i_5 i_6}^{a_1} T_{i_3 i_4}^{a_2}, & \mathcal{C}_5 &= \delta_{i_5 i_6} (T^{a_1} T^{a_2})_{i_3 i_4}, & \mathcal{C}_6 &= \delta_{i_5 i_6} (T^{a_2} T^{a_1})_{i_3 i_4}, \\ \mathcal{C}_7 &= T_{i_3 i_6}^{a_1} T_{i_5 i_4}^{a_2}, & \mathcal{C}_8 &= \delta_{i_3 i_6} (T^{a_1} T^{a_2})_{i_5 i_4}, & \mathcal{C}_9 &= \delta_{i_3 i_6} (T^{a_2} T^{a_1})_{i_5 i_4}, \\ \mathcal{C}_{10} &= T_{i_5 i_4}^{a_1} T_{i_3 i_6}^{a_2}, & \mathcal{C}_{11} &= \delta_{i_5 i_4} (T^{a_1} T^{a_2})_{i_3 i_6}, & \mathcal{C}_{12} &= \delta_{i_5 i_4} (T^{a_2} T^{a_1})_{i_3 i_6}, \\ \mathcal{C}_{13} &= \delta^{a_1 a_2} \delta_{i_3 i_4} \delta_{i_5 i_6}, & \mathcal{C}_{14} &= \delta^{a_1 a_2} \delta_{i_3 i_6} \delta_{i_5 i_4}. \end{aligned} \quad (2.5)$$

For $N_c = 3$, only 13 of these colour operators are independent owing to the relation

$$\mathcal{C}_{14} = -2 \sum_{i=1}^6 \mathcal{C}_i + 2 \sum_{i=7}^{12} \mathcal{C}_i + \mathcal{C}_{13}. \quad (2.6)$$

The summation over external colours is performed once and for all at the level of the colour basis and the LO matrix element. To this end, we compute the colour-interference matrix

$$I_{kl} = \sum_{\text{col}} \mathcal{C}_k \mathcal{C}_l^*, \quad (2.7)$$

and reducing the tree matrix element in colour space,

$$\mathcal{M}^{(\text{LO})} = \sum_l \mathcal{M}_l^{(\text{LO})} \mathcal{C}_l, \quad (2.8)$$

we build the interference of $\mathcal{M}^{(\text{LO})}$ with the elements of the colour basis as

$$\tilde{\mathcal{M}}_k^{(\text{LO})} = \sum_{\text{col}} \mathcal{C}_k \left(\mathcal{M}^{(\text{LO})} \right)^* = \sum_l I_{kl} \left(\mathcal{M}_l^{(\text{LO})} \right)^*. \quad (2.9)$$

Then, upon reduction of the factorized colour structure of the loop diagrams,

$$\mathcal{M}^{(\Gamma)} = \mathcal{A}^{(\Gamma)} \mathcal{C}^{(\Gamma)} = \mathcal{A}^{(\Gamma)} \left(\sum_k c_k^{(\Gamma)} \mathcal{C}_k \right), \quad (2.10)$$

we obtain the colour-summed loop–tree interference as

$$\sum_{\text{col}} \mathcal{M}^{(\Gamma)} \left(\mathcal{M}^{(\text{LO})} \right)^* = \mathcal{A}^{(\Gamma)} \left(\sum_k c_k^{(\Gamma)} \tilde{\mathcal{M}}_k^{(\text{LO})} \right), \quad (2.11)$$

where the coefficients $c_k^{(\Gamma)}$ are simple numbers. The colour-summed result is given by a combination of previously computed colour–Born interference terms (2.9). This requires a *single evaluation* of the non-trivial colour-stripped amplitude $\mathcal{A}^{(\Gamma)}$ of each (sub)diagram.

Helicity structures are handled in a very similar way. The helicity-dependent parts of all diagrams are reduced to a common basis of so-called Standard Matrix Elements (SMEs), and helicity sums are performed once and for all at the level of the SMEs–Born interference (see below). The diagram-independent treatment of the helicity-dependent parts of loop graphs is made possible by the covariant decomposition of tensor integrals, i.e. by replacing loop momenta (in the numerator) with external momenta and metric tensors.

Covariant decomposition and numerical reduction of tensor integrals

Tensor one-loop integrals with N propagators and P Lorentz indices are expressed in terms of totally symmetric covariant structures $\{g \dots gp \dots p\}_{j_1 \dots j_P}^{\mu_1 \dots \mu_P}$ involving $g^{\mu\nu}$ and the external momenta p_1, \dots, p_{N-1} ,

$$\frac{(2\pi\mu)^{4-D}}{i\pi^2} \int d^D q \frac{q^{\mu_1} \dots q^{\mu_P}}{\prod_{i=0}^{N-1} [(q + p_i)^2 - m_i^2 + i0]} = \sum_{j_1, \dots, j_P=0}^{N-1} T_{j_1 \dots j_P}^N \{g \dots gp \dots p\}_{j_1 \dots j_P}^{\mu_1 \dots \mu_P}, \quad (2.12)$$

with D denoting the number of space–time dimensions. For details of the notation we refer to Ref. [21]. To describe N -point integrals with $N \geq 5$, tensor structures with only four external momenta would be sufficient. However, in order to avoid potential instabilities due to inverse Gram determinants we use a redundant set of structures, including the metric tensor and $N - 1$ momenta.

The virtual corrections to $q\bar{q} \rightarrow t\bar{t}b\bar{b}$ and $gg \rightarrow t\bar{t}b\bar{b}$ involve tensor integrals up to rank $P = 3$ and $P = 4$, respectively. The one-loop amplitudes are expressed as linear combinations of tensor-integral coefficients T_{j_1, \dots, j_P}^N . The latter are evaluated by *numerical* libraries that recursively reduce them to master integrals using the methods of Refs. [20, 21]². Avoiding an explicit reduction of analytic expressions to master integrals,

²We note in passing that the reduction methods of Refs. [20, 21] have also been used in the related calculation [62] of NLO QCD corrections to the $2 \rightarrow 4$ particle process $\gamma\gamma \rightarrow t\bar{t}b\bar{b}$ at a $\gamma\gamma$ collider.

this numerical approach prevents prohibitively large expressions and permits to adapt the reduction strategy to the specific numerical problems that appear in different phase-space regions.

Tensor N -point integrals with $N \geq 5$ are expressed in terms of lower-rank and lower-point integrals exploiting the four-dimensionality of space–time [20,21].³ The tensor rank and the number of propagators are simultaneously reduced without introducing inverse Gram determinants. Consequently, the maximal power of inverse Gram determinants resulting from the entire reduction is given by the maximal rank of four-point integrals, which never exceeds four in renormalizable gauges. Scalar hexagons and pentagons are reduced to boxes using Melrose’s method [60]. Tensor 4-point and 3-point integrals are reduced to scalar integrals with the Passarino–Veltman algorithm [61] as long as no small Gram determinant appears in the reduction. If small Gram determinants occur, alternative schemes are applied [21].⁴ More precisely, we make use of expansions of the tensor coefficients about the limit of vanishing Gram determinants and possibly other kinematical determinants. One- and two-point tensor integrals are obtained with numerically stable analytic expressions.

Ultraviolet (UV) divergences are regularized dimensionally throughout, but infrared (IR) divergences are treated in different variants, which comprise pure dimensional regularization with strictly massless light quarks and a hybrid scheme with small quark masses. The corresponding scalar integrals are evaluated using the methods and results of Refs. [63,64], and different regularization schemes are translated into each other as described in Ref. [65].

The calculation of tensor integrals is implemented in two independent FORTRAN libraries. This permits to perform detailed cross checks, which confirm the excellent numerical stability of the reduction procedure. An automatic cache system is implemented that strongly boosts the reduction by recycling a multitude of tensor integrals among Feynman diagrams with common sub-topologies. The virtual corrections to $gg \rightarrow t\bar{t}b\bar{b}$ comprise about 350 different scalar integrals, which require roughly 10 ms CPU time per phase-space point on a 3 GHz Intel Xeon processor. The calculation of the complete set of scalar and tensor integrals with and without cache system takes approximately 40 ms and 200 ms, respectively.

Rational parts

In $D = 4 - 2\epsilon$ dimensions, UV-singular tensor integrals give rise to $1/\epsilon_{\text{UV}}$ poles,

$$T_{j_1 \dots j_P}^N = \hat{T}_{j_1 \dots j_P}^N + \frac{R_{j_1 \dots j_P}^N}{\epsilon_{\text{UV}}}. \quad (2.13)$$

Consequently, their D -dimensional coefficients need to be expanded in $D - 4$,

$$f(D)T_{j_1 \dots j_P}^N = f(4)T_{j_1 \dots j_P}^N - 2f'(4)R_{j_1 \dots j_P}^N, \quad (2.14)$$

resulting in so-called rational terms that are proportional to the pole residues $R_{j_1 \dots j_P}^N$. Rational contributions originate from D -dependent terms in tensor-reduction identities

³Similar reductions are described in Ref. [25].

⁴Similar procedures based on numerical evaluations of specific one-loop integrals [19,25] or expansions in small determinants [24] have also been proposed by other authors.

and in the loop-momentum-independent part of the diagram numerators. The relevant expansions are automatically performed by means of a catalogue of residues of UV poles.

Note that in (2.14) we have implicitly assumed that rational terms resulting from $1/\epsilon$ and $1/\epsilon^2$ poles of IR kind vanish. This is a non-trivial and general property of one-loop QCD amplitudes. More precisely, while rational terms of IR origin can be present in the wave-function renormalization factors, in truncated one-loop amplitudes they cancel. This holds within the 't Hooft–Feynman gauge and similar gauge fixings, as was explicitly proven in Appendix A of Ref. [10].

Algebraic reduction of helicity structures and helicity sums

The helicity structures encountered in the explicit evaluation of all Feynman diagrams are algebraically reduced to a common basis of SMEs as described below. The general form of SMEs for the $gg \rightarrow t\bar{t}b\bar{b}$ channel is⁵

$$\hat{\mathcal{M}}_m = Q_m^{\mu_1\mu_2\rho_1\dots\rho_l} \varepsilon_{\mu_1}(p_1) \varepsilon_{\mu_2}(p_2) [\bar{v}(p_3) \gamma_{\rho_1} \dots \gamma_{\rho_k} u(p_4)] [\bar{v}(p_5) \gamma_{\rho_{k+1}} \dots \gamma_{\rho_l} u(p_6)], \quad (2.15)$$

where $Q_m^{\mu_1\mu_2\rho_1\dots\rho_l}$ consists of combinations of metric tensors and external momenta. These compact spinor chains permit to decouple helicity information from the remnant parts of the diagrams, so that helicity sums can be performed in a diagram-independent and efficient way. In practice, the colour-stripped part of each loop diagram [see (2.10)] is expressed as a linear combination of SMEs and tensor integrals,

$$\begin{aligned} \mathcal{A}^{(\Gamma)} &= \sum_m \mathcal{F}_m^{(\Gamma)} \hat{\mathcal{M}}_m, \\ \mathcal{F}_m^{(\Gamma)} &= \sum_P \sum_{j_1, \dots, j_P=0}^{N-1} \mathcal{K}_{m; j_1 \dots j_P}^{(\Gamma)} T_{j_1 \dots j_P}^N + \text{rational parts}. \end{aligned} \quad (2.16)$$

The coefficients $\mathcal{K}_{m; i_1 \dots i_P}^{(\Gamma)}$ are rational functions of the kinematic invariants. These functions involve only denominators from intermediate-particle propagators and are free of spurious poles that might generate numerical instabilities.

Helicity sums are performed at the level of the interference of the diagram-independent SMEs with the colour-projected Born amplitude (2.9),

$$M_{km} = \sum_{\text{hel}} \hat{\mathcal{M}}_m \tilde{\mathcal{M}}_k^{(\text{LO})} = \sum_l I_{kl} \sum_{\text{hel}} \hat{\mathcal{M}}_m \left(\mathcal{M}_l^{(\text{LO})} \right)^*. \quad (2.17)$$

This matrix is computed only once per phase-space point employing the Weyl–van der Waerden spinor formalism of Ref. [68]. Using M_{km} one can directly obtain the colour- and helicity-summed contributions of each loop diagram in terms of its colour- and helicity-independent form factors $\mathcal{F}_m^{(\Gamma)}$ and the coefficients $c_k^{(\Gamma)}$ of its factorized colour structure (2.10),

$$\sum_{\text{col}} \sum_{\text{hel}} \mathcal{M}^{(\Gamma)} \left(\mathcal{M}^{(\text{LO})} \right)^* = \sum_m \mathcal{F}_m^{(\Gamma)} \left(\sum_k c_k^{(\Gamma)} M_{km} \right). \quad (2.18)$$

⁵For convenience we consider the crossed process $gg\bar{t}\bar{t}b\bar{b} \rightarrow 0$, i.e. we treat all particles and momenta as incoming.

Owing to the high number of SMEs $\hat{\mathcal{M}}_m$ and the complexity of the corresponding form factors $\mathcal{F}_m^{(\Gamma)}$, the representation (2.18) yields fairly large expressions. For instance, the size of the numerical routines describing individual hexagon diagrams in the gg channel is of the order of 0.5–1 MB. The reduction of helicity structures to SMEs is one of the key aspects that determine the size and the speed of the code. In order to avoid possible numerical cancellations, this procedure is entirely based on algebraic identities that are free of denominators. The reduction algorithm consists of two main steps. The first step is based on process-independent identities in D dimensions. To reduce helicity structures of type (2.15) we employ: momentum conservation; Dirac algebra; ordering of Dirac matrices inside Dirac chains; Dirac equation; transversality and gauge-fixing conditions for the gluon-polarization vectors, $p_i^\mu \varepsilon_\mu(p_j) = 0$ for $i, j = 1, 2$. The basis of SMEs obtained with these identities contains more than thousand elements for the gg channel.

After these manipulations in D dimensions we extract all rational terms performing the relevant expansions in $D - 4$. We then proceed with a second reduction step, based on four-dimensional relations. Specifically, we apply two alternative reduction algorithms that are based on relations derived from Chisholm's identity.

The first algorithm is constructed along the lines of the reduction described in Ref. [10] for the $q\bar{q}$ channel. Each fermion chain is split into two contributions via insertion of chiral projectors $\omega_\pm = (1 \pm \gamma^5)/2$,

$$[\bar{v}(p_3)\Gamma_a u(p_4)][\bar{v}(p_5)\Gamma_b u(p_6)] = \sum_{\lambda, \rho=\pm} [\bar{v}(p_3)\Gamma_a \omega_\lambda u(p_4)][\bar{v}(p_5)\Gamma_b \omega_\rho u(p_6)]. \quad (2.19)$$

This permits to employ various relations of the type [10, 66]

$$\gamma^\mu \gamma^\alpha \gamma^\beta \omega_\pm \otimes \gamma_\mu = \gamma^\mu \omega_\pm \otimes (\gamma_\mu \gamma^\beta \gamma^\alpha \omega_\pm + \gamma^\alpha \gamma^\beta \gamma_\mu \omega_\mp), \quad (2.20)$$

where the tensor product connects Dirac matrices that belong to different fermion chains. By means of such identities one can exchange Dirac matrices between chains that are connected by $\gamma^\mu \otimes \gamma_\mu$ contractions. As described in Ref. [10], using identities of type (2.20) in combination with the above-mentioned D -dimensional relations (Dirac equation, etc.) one can obtain a rich variety of non-trivial reduction identities. In this way we have constructed a fairly sophisticated reduction algorithm (see App. A) that relates all helicity structures present in the gg channel to 502 SMEs. In spite of its efficiency, this reduction procedure has the disadvantage of depending on process-specific aspects, like the number of massive and massless fermion chains and the number of external momenta. It is thus important to investigate the trade-off between the obtained efficiency and the time-consuming task of designing the reduction on a process-by-process basis. To this end, we have implemented an alternative and much simpler reduction method. This procedure is entirely process-independent. It does not make use of chiral projectors, and consists of a single four-dimensional identity,

$$\begin{aligned} \gamma^{\mu_1} \gamma^{\mu_2} \gamma^{\mu_3} \gamma^{\mu_4} \gamma^{\mu_5} &= g^{\mu_1 \mu_2} \gamma^{\mu_3} \gamma^{\mu_4} \gamma^{\mu_5} - g^{\mu_1 \mu_3} \gamma^{\mu_2} \gamma^{\mu_4} \gamma^{\mu_5} + g^{\mu_1 \mu_4} \gamma^{\mu_2} \gamma^{\mu_3} \gamma^{\mu_5} - g^{\mu_1 \mu_5} \gamma^{\mu_2} \gamma^{\mu_3} \gamma^{\mu_4} \\ &+ g^{\mu_2 \mu_3} \gamma^{\mu_1} \gamma^{\mu_4} \gamma^{\mu_5} - g^{\mu_2 \mu_4} \gamma^{\mu_1} \gamma^{\mu_3} \gamma^{\mu_5} + g^{\mu_2 \mu_5} \gamma^{\mu_1} \gamma^{\mu_3} \gamma^{\mu_4} + g^{\mu_3 \mu_4} \gamma^{\mu_1} \gamma^{\mu_2} \gamma^{\mu_5} \\ &- g^{\mu_3 \mu_5} \gamma^{\mu_1} \gamma^{\mu_2} \gamma^{\mu_4} + g^{\mu_4 \mu_5} \gamma^{\mu_1} \gamma^{\mu_2} \gamma^{\mu_3} - (g^{\mu_1 \mu_2} g^{\mu_3 \mu_4} - g^{\mu_1 \mu_3} g^{\mu_2 \mu_4} + g^{\mu_1 \mu_4} g^{\mu_2 \mu_3}) \gamma^{\mu_5} \\ &+ (g^{\mu_1 \mu_2} g^{\mu_3 \mu_5} - g^{\mu_1 \mu_3} g^{\mu_2 \mu_5} + g^{\mu_1 \mu_5} g^{\mu_2 \mu_3}) \gamma^{\mu_4} - (g^{\mu_1 \mu_2} g^{\mu_4 \mu_5} - g^{\mu_1 \mu_4} g^{\mu_2 \mu_5} \\ &+ g^{\mu_1 \mu_5} g^{\mu_2 \mu_4}) \gamma^{\mu_3} + (g^{\mu_1 \mu_3} g^{\mu_4 \mu_5} - g^{\mu_1 \mu_4} g^{\mu_3 \mu_5} + g^{\mu_1 \mu_5} g^{\mu_3 \mu_4}) \gamma^{\mu_2} - (g^{\mu_2 \mu_3} g^{\mu_4 \mu_5} \\ &- g^{\mu_2 \mu_4} g^{\mu_3 \mu_5} + g^{\mu_2 \mu_5} g^{\mu_3 \mu_4}) \gamma^{\mu_1}, \end{aligned} \quad (2.21)$$

which can be derived from Chisholm’s identity and permits to eliminate any spinor chain involving more than three Dirac matrices without introducing γ_5 and ϵ -tensors.⁶ In this case we could reduce all gg-channel helicity structures to 970 SMEs.

Comparing the number of SMEs obtained with the process-dependent and process-independent algorithms, we observe that the former is superior by roughly a factor two. Thus, if we naively assume that the CPU efficiency scales with the number of SMEs, we would expect a factor-two difference in the speed of the numerical code. In contrast, we find that the CPU efficiency obtained with the two reductions is almost identical. This suggests that the reduction of the number of SMEs is compensated by an increase in the size of the form factors. This unexpected result means that the obtained CPU performance—at least for this process—does not depend on sophisticated and process-dependent optimisations.

2.2 Real corrections

The calculation of the $q\bar{q}$ channel has been described in Ref. [11]. The evaluation of the $(\bar{q})g$ channels is done in the same way. In the following we sketch the calculation for the gg channel. We have again performed two independent calculations of all building blocks.

In both evaluations of the real corrections the amplitudes are calculated as helicity matrix elements which have been generated with MADGRAPH 4.1.33 [67]. While the amplitudes for $q\bar{q} \rightarrow t\bar{t}b\bar{b}g$ and $(\bar{q})g \rightarrow t\bar{t}b\bar{b}(\bar{q})$ have been checked with the Weyl–van der Waerden spinor formalism of Ref. [68], those for $gg \rightarrow t\bar{t}b\bar{b}g$ have been verified with an implementation of off-shell recursion relations [69–71]. The singularities for soft and collinear gluon emission are isolated via dipole subtraction [50–53] for NLO QCD calculations using the formulation [53] for massive quarks. Soft and collinear singularities in the “endpoint part” of the subtraction function (the I operator of Refs. [50, 53]), i.e. the part of the subtraction terms that has to be combined with the virtual corrections, are regularized using the same regularization prescription (dimensional or with small quark masses) as the corresponding virtual corrections. No regularization is needed in the subtraction terms for the real corrections. For both the $q\bar{q}$ and gg channels 30 different dipole subtraction terms need to be included while each $(\bar{q})g$ channel requires only 10, since we demand b quarks with finite transverse momentum in the final state. After combining virtual and real corrections, singularities connected to collinear configurations in the final state cancel for “collinear-safe” observables after applying a jet algorithm. Singularities connected to collinear initial-state splittings are removed via $\overline{\text{MS}}$ QCD factorization by PDF redefinitions. In both evaluations the phase-space integration is performed with multi-channel Monte Carlo generators [54] and adaptive weight optimisation similar to the one implemented in LUSIFER [56].

Version 1 of the real corrections employs the MADDIPOLE implementation of dipole subtraction [72]. The phase-space integration, implemented in C++, is based on RACOONWW, but the phase-space mappings are built up in a more generic way very

⁶ Products of four Dirac matrices can occur only inside the massive top-quark chain. In this case one can introduce a fifth Dirac matrix by rewriting the massive spinor as $u(p) = \not{p}u(p)/m$, and then use (2.21).

	$\sigma/\sigma_{\text{LO}}$	# events (after cuts)	$(\Delta\sigma)_{\text{stat}}/\sigma$	runtime	time/event
tree level	86%	5.3×10^6	0.4×10^{-3}	38 min	0.4 ms
virtual	-11%	0.26×10^6	0.6×10^{-3}	13 h	180 ms
real + dipoles	49%	10×10^6	3×10^{-3}	40 h	14 ms
total	124%		4×10^{-3}	53 h	

Table 1: Statistics and speed of various parts of the calculation based on 2×10^7 events before applying cuts generated on a 3 GHz Intel Xeon processor using the pgf77 compiler with standard options.

similar to the approach of LUSIFER [56]. For each of the 341 bremsstrahlung Feynman diagrams a corresponding channel is taken into account in the Monte Carlo integration.

In *version 2* all dipole subtraction terms have been implemented directly into the Monte Carlo generator. The Monte Carlo generator is a further development of the one used in COFFER $\gamma\gamma$ [73] and for the calculation of the NLO corrections to $pp \rightarrow H_{jj} + X$ [74]. In addition to the Monte Carlo channels for the bremsstrahlung diagrams $30 \times 36 = 1080$ channels are used to map the dipole subtraction terms in the gg channel. These additional channels lead to some improvement in the convergence of the Monte Carlo integration.

All real bremsstrahlung amplitudes of Madgraph have been checked against independent calculations for several phase-space points. The cancellation between real matrix elements and dipole subtraction terms has been verified numerically in all soft and collinear regions. The individual dipole subtraction terms, the subtracted real matrix elements, and the integrated subtraction terms (P and K terms of Refs. [50, 53]) have been compared point-wise between the two independent calculations. The agreement was generally at the level of 13 digits. The integrated LO cross section has been verified with SHERPA [75] at the level of the integration errors of 0.2%. From the point of view of Monte Carlo integration the most complicated and time-consuming part is the integration of the real corrections in the gg channel. For the complete NLO cross section we found agreement between the two versions of our code within $1-3\sigma$, where 1σ corresponds to 0.1–0.2%. The results for the distributions coincide within $1-3\sigma$ for each bin.

In order to give an impression on the statistics and the required CPU time we show in Table 1 some numbers for 2×10^7 generated phase-space points before cuts. This yields an accuracy for the NLO cross section of about 0.5%. The contributions of the $(\bar{q})g$ channel were calculated for every 4th event and those of the virtual corrections in the gg channel and the contributions of the $q\bar{q}$ channel for every 20th event. The bulk of the runtime is taken by the gg channel. For the virtual corrections the CPU time is dominated by the gg channel and amounts to 180 ms per event. The virtual correction in the $q\bar{q}$ channel are by a factor 20 faster. In order to produce the plots for the scale variations we generated 2×10^7 phase-space points for the NLO predictions and 2×10^8 for the LO cross section. To generate the distributions we used about 20 times more events for the NLO results.

3 Predictions for the LHC

The thorough description of a complex signature like $t\bar{t}b\bar{b}$ involves numerous possible observables. Here we investigate distributions and cuts that are relevant for the search of $t\bar{t}H(H \rightarrow b\bar{b})$ at the LHC [5, 7], where $t\bar{t}b\bar{b}$ contributes to the irreducible background. In our previous work [11] we found a K factor of about 1.8 for the integrated $t\bar{t}b\bar{b}$ cross section at the LHC. This unexpectedly large NLO effect raises two important issues that we address in the present analysis. Firstly, we discuss the relation between the large K factor and the scale choice. This leads us to a new and more appropriate scale choice, which improves the convergence of the perturbative expansion. Secondly, we consider possible strategies to reduce the $t\bar{t}b\bar{b}$ cross section in order to facilitate the extraction of the $t\bar{t}H$ signal. In particular, we study the influence of a jet veto on the NLO cross section and its perturbative stability. We also explore the kinematic region of highly-boosted $b\bar{b}$ pairs, which helps to separate the Higgs signal from its QCD background, as first suggested for associated WH and ZH production [8] and, very recently, also for $t\bar{t}H$ production [9].

Let us remind that top-quark decays are not included in our calculation. In practice we treat top quarks in a completely inclusive way, and we restrict our analysis to the kinematic properties of those two b quarks that do not result from top decays. From the experimental view-point, the presented distributions correspond to the unrealistic situation of perfect top-quark reconstruction. The detailed description of top-decay products and the related issue of b-quark combinatorics are left for future studies.

3.1 Input parameters, jet definition, and cuts

We study the process $pp \rightarrow t\bar{t}b\bar{b} + X$ at $\sqrt{s} = 14 \text{ TeV}$. For the top-quark mass, renormalized in the on-shell scheme, we take the numerical value $m_t = 172.6 \text{ GeV}$ [76]. All other QCD partons, including b quarks, are treated as massless particles. Collinear final-state configurations, which give rise to singularities, are recombined into IR-safe jets using a k_T -algorithm [77]. Specifically, we adopt the k_T -algorithm of Ref. [78] and recombine all final-state b quarks and gluons with pseudorapidity $|\eta| < 5$ into jets with separation $\sqrt{\Delta\phi^2 + \Delta y^2} > D = 0.4$ in the rapidity–azimuthal-angle plane. Requiring two b jets, this also avoids collinear singularities resulting from massless $g \rightarrow b\bar{b}$ splittings.⁷

After recombination, we impose the following cuts on the transverse momenta and rapidities of the b jets:

$$p_{T,b} > p_{T,b,\text{cut}} = 20 \text{ GeV}, \quad |y_b| < y_{b,\text{cut}} = 2.5. \quad (3.1)$$

This choice is dictated by the detector geometry and the search for a $t\bar{t}H(H \rightarrow b\bar{b})$ signal at the LHC [5, 7]. The outgoing (anti)top quarks are neither affected by the jet algorithm nor by phase-space cuts. For what concerns b quarks, the jet algorithm and the requirement of having two b jets with $p_{T,b} > 20 \text{ GeV}$ sets an effective lower limit on the $b\bar{b}$ invariant mass of roughly 10 GeV. But the $m_{b\bar{b}}$ -range that is relevant for the Higgs-boson search is actually much higher. In this kinematic region, with $p_{T,b} \gg m_b$ and $m_{b\bar{b}} \gg m_b$,

⁷ Note that, as compared to our previous analysis [10, 11], we have reduced the jet-algorithm parameter from $D = 0.8$ to $D = 0.4$. This is particularly important for highly boosted b-quark pairs with $m_{b\bar{b}} \sim M_H$, since $D = 0.8$ would lead to their recombination into a single jet and, consequently, to their rejection.

we expect that the $m_b = 0$ approximation works fairly well. To assess its precision we compared the LO cross section for $m_b = 0$ and $m_b = 4.2$ GeV using SHERPA [75]. For the integrated cross section, which is dominated by $m_{b\bar{b}}$ values well below 100 GeV, we found that the finite- m_b effect is smaller than 3%.

We consistently use the CTEQ6 [79] set of PDFs, i.e. we take CTEQ6L1 PDFs with a one-loop running α_s in LO and CTEQ6M PDFs with a two-loop running α_s in NLO, but neglect the suppressed contributions from b quarks in the initial state. The number of active flavours is $N_F = 5$, and the respective QCD parameters are $\Lambda_5^{\text{LO}} = 165$ MeV and $\Lambda_5^{\overline{\text{MS}}} = 226$ MeV. In the renormalization of the strong coupling constant the top-quark loop in the gluon self-energy is subtracted at zero momentum. In this scheme, the running of α_s is generated solely by the contributions of the light-quark and gluon loops.

3.2 Renormalization and factorization scales

The perturbative expansion of the $pp \rightarrow t\bar{t}b\bar{b}$ cross section starts with the fourth power of α_s . Consequently the LO predictions, and also the K factor, are extremely sensitive to variations of the renormalization scale. In Ref. [4] it was pointed out that the LO $t\bar{t}b\bar{b}$ cross section can vary by up to a factor four if the QCD scale is identified with different kinematic parameters. In all recent ATLAS studies of $t\bar{t}H(H \rightarrow b\bar{b})$ [2, 4, 5] the signal and its $t\bar{t}b\bar{b}$ background were simulated by setting the renormalization and factorization scales equal to half the threshold energy, $E_{\text{thr}} = 2m_t + m_{b\bar{b}}$. For $pp \rightarrow t\bar{t}H + X$, this choice was well supported by the existing NLO analysis [13, 14]. But, in the absence of NLO predictions for $t\bar{t}b\bar{b}$, the choice of the same scale for signal and background was motivated solely by the assumption that the two processes have similar kinematics. However, in Ref. [11] we found that, if both processes are evaluated at $\mu_R = \mu_F = E_{\text{thr}}/2$, $pp \rightarrow t\bar{t}b\bar{b}$ receives much larger NLO corrections ($K \simeq 1.8$) than $pp \rightarrow t\bar{t}H$ ($K \simeq 1.2$). This is mainly due to the fact that the scale $E_{\text{thr}}/2$ does not provide an adequate description of the QCD dynamics that governs $t\bar{t}b\bar{b}$ production.

The main difference between $pp \rightarrow t\bar{t}H(H \rightarrow b\bar{b})$ and its irreducible QCD background is that the former process involves only two powers of α_s at LO. Moreover, the part of the signal process that is mediated by strong interactions does not involve any scale significantly smaller than $E_{\text{thr}}/2$. In contrast, $pp \rightarrow t\bar{t}b\bar{b}$ is entirely driven by QCD and is proportional to α_s^4 at LO. In the $m_{b\bar{b}} \rightarrow 0$ limit, the dominant $t\bar{t}b\bar{b}$ production mechanism is $pp \rightarrow t\bar{t}g(g \rightarrow b\bar{b})$, where a gluon with small virtuality plays a role analogous to the intermediate Higgs boson in the signal process. In this regime, the factorization of $t\bar{t}g$ production and $g \rightarrow b\bar{b}$ splitting provides two well-defined and widely separated scales: $E_{\text{thr}}/2$ and $m_{b\bar{b}}$, respectively. This simple picture is, however, not applicable to the kinematic region of interest, where $m_{b\bar{b}} \gtrsim 100$ GeV. Here, $pp \rightarrow t\bar{t}b\bar{b}$ involves various other mechanisms. For instance, the radiation of one or both b quarks off initial-state gluons can play an important role due to collinear enhancements. In order to find an optimal QCD scale, we have tried to identify a dominant production mechanism. To this end, we have inspected the relative weights of the channels corresponding to various Feynman-diagram topologies in our adaptive Monte Carlo generator. However, we found that none of these channels is strongly enhanced with respect to the others. Similarly we were not able to reproduce the bulk of the cross section in terms of effective approximations

Setup	$m_{b\bar{b},\text{cut}}$	$p_{T,b\bar{b},\text{cut}}$	$p_{\text{jet,veto}}$	$p_{T,b,\text{cut}}$	$y_{b,\text{cut}}$	σ_{LO}	σ_{NLO}	K
I	100	-	-	20	2.5	786.3(2) ^{+78%} _{-41%}	978(3) ^{+13%} _{-21%}	1.24
II	-	200	-	20	2.5	451.8(2) ^{+79%} _{-41%}	592(4) ^{+13%} _{-22%}	1.31
III	100	-	100	20	2.5	786.1(6) ^{+78%} _{-41%}	700(3) ^{+0.4%} _{-19%}	0.89
IV	100	-	-	50	2.5	419.4(1) ^{+77%} _{-40%}	526(2) ^{+13%} _{-21%}	1.25

Table 2: Cut parameters (in GeV), integrated LO and NLO cross section (in fb) with statistical errors and scale variations by factors 2 up and down as well as K factors for the four different setups.

based on collinear $g \rightarrow b\bar{b}$ splittings of the incoming gluons. This suggests that $pp \rightarrow t\bar{t}b\bar{b}$ is a genuinely multi-scale and multi-channel reaction.

We thus decided to adopt a pragmatic scale choice, based on the kinematic properties of the $t\bar{t}b\bar{b}$ final state. While m_t sets a clear scale for the couplings to the top quarks, the inspection of differential distributions reveals that the cross section is saturated by b quarks with $p_{T,b} \ll m_t$ (see Figs. 8 and 9). In order to account for these different scales we have adopted a dynamical QCD scale corresponding to their geometric average,

$$\mu_0^2 = m_t \sqrt{p_{T,b} p_{T,\bar{b}}}. \quad (3.2)$$

Our LO and NLO predictions are obtained by varying the renormalization (μ_R) and factorization (μ_F) scales around the central value (3.2),

$$\mu_R = \xi_R \mu_0, \quad \mu_F = \xi_F \mu_0. \quad (3.3)$$

In the following sections we investigate the dependence of the LO and NLO integrated cross section with respect to uniform ($\xi_F = \xi_R$) and antipodal ($\xi_F = \xi_R^{-1}$) scale variations in the range $1/8 \leq \xi_F, \xi_R \leq 8$. We find that uniform variations have a larger impact on the cross section as compared to antipodal variations. For all distributions we provide LO and NLO predictions with uncertainty bands corresponding to factor-two uniform scale variations. More precisely, all observables are evaluated at three different scales: $\xi_F = \xi_R = 0.5, 1, 2$. As we will see from the reduction of the K factor and the scale uncertainties, the scale choice (3.2) clearly improves the convergence of the perturbative expansion as compared to Ref. [11].

3.3 Additional cuts

Besides the standard cuts (3.1), we have imposed the following kinematic restrictions to the $b\bar{b}$ system and the extra jet that is radiated at NLO:

$$m_{b\bar{b}} > m_{b\bar{b},\text{cut}}, \quad p_{T,b\bar{b}} > p_{T,b\bar{b},\text{cut}}, \quad p_{T,\text{jet}} < p_{\text{jet,veto}}. \quad (3.4)$$

In order to investigate the individual effect of these extra cuts and correlations with other observables, we have generated differential distributions in four different setups described in Table 2. The setups I–III implement the standard cuts (3.1) and explore the individual impact of the extra cuts (3.4). Setup IV is a variant of setup I, where the cut (3.1) on the b -jet p_T is increased from 20 GeV to 50 GeV.

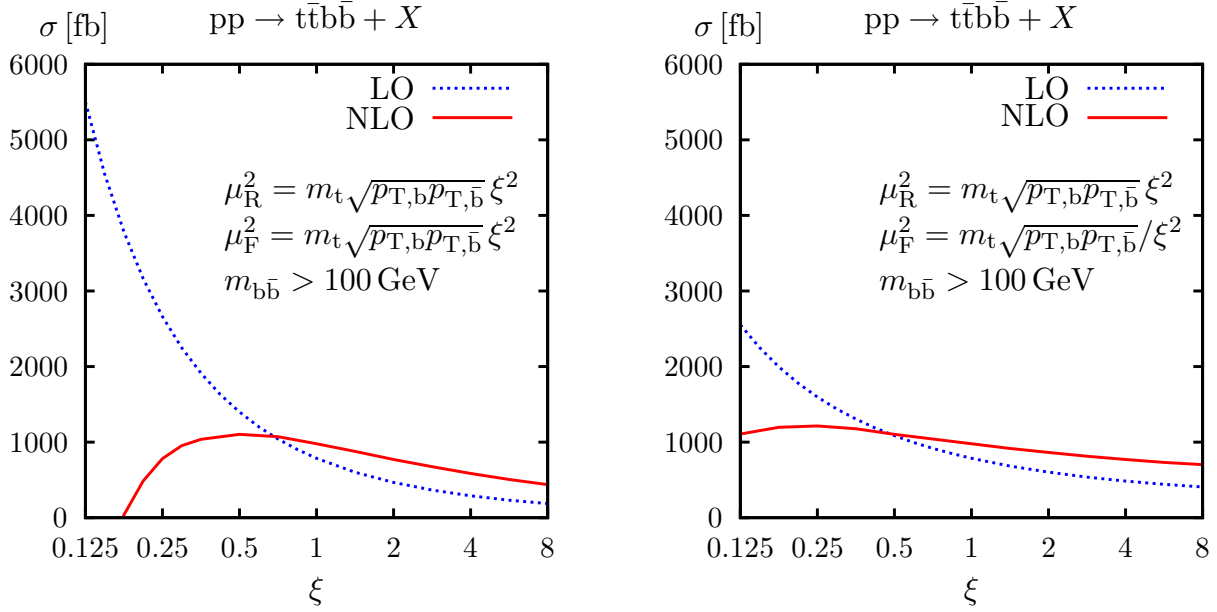


Figure 4: Scale dependence of the LO and NLO $pp \rightarrow t\bar{t}b\bar{b} + X$ cross section at $\sqrt{s} = 14$ TeV in setup I. The left and the right plots describe uniform ($\xi_R = \xi_F = \xi$) and antipodal ($\xi_R = \xi_F^{-1} = \xi$) scale variations, respectively.

3.4 Setup I

In this setup we impose the cut $m_{b\bar{b}} > 100$ GeV. This removes a large part of the cross section and selects the kinematic region of interest for the $t\bar{t}H(H \rightarrow b\bar{b})$ signal.

Scale dependence

The LO and NLO integrated cross sections and their dependence with respect to uniform (left plot) and antipodal (right plot) scale variations are displayed in Figure 4. At the central scale we obtain $\sigma_{\text{LO}} = 786.3(2)$ fb and $\sigma_{\text{NLO}} = 978(3)$ fb, where the numbers in parentheses are the errors of the Monte Carlo integration for 2×10^8 LO events and 2×10^7 NLO events before applying cuts. These predictions are not directly comparable to those of Ref. [11], where we did not apply any cut to $m_{b\bar{b}}$. Still we can compare the K factors, which are rather insensitive to $m_{b\bar{b}}$. We observe that the new scale choice (3.2) reduces the NLO corrections from $K \simeq 1.77$ [11] to $K \simeq 1.24$. We note that, in spite of the smaller K factor, the new scale choice yields larger LO and NLO cross sections as compared to the scale $E_{\text{thr}}/2$ used in Ref. [11]. This can be easily seen from Figure 4, where the new and the previous central scales correspond to $\mu_R/\mu_0 = 1$ and $\mu_R/\mu_0 = E_{\text{thr}}/(2\mu_0) \gg 1$, respectively.⁸ In addition to the K factor, the new scale choice reduces also the NLO scale uncertainty. Varying the scale up or down by a factor 2 changes the LO and NLO cross section by 78% in LO and by 21% in NLO. The improvement with

⁸ Using setup-I cuts and the ATLAS scale choice $\mu_{R,F} = E_{\text{thr}}/2$ we obtain $\sigma_{\text{LO}}(E_{\text{thr}}/2) = 448.7(1)$ fb and $\sigma_{\text{NLO}}(E_{\text{thr}}/2) = 751(2)$ fb. The increase of the cross section due to the combined effect of the new scale choice and the NLO correction factor is thus $\sigma_{\text{NLO}}(\mu_0)/\sigma_{\text{LO}}(E_{\text{thr}}/2) \simeq 2.18$ while the K factor for setup-I cuts and the ATLAS scale choice results in $K \simeq 1.67$.

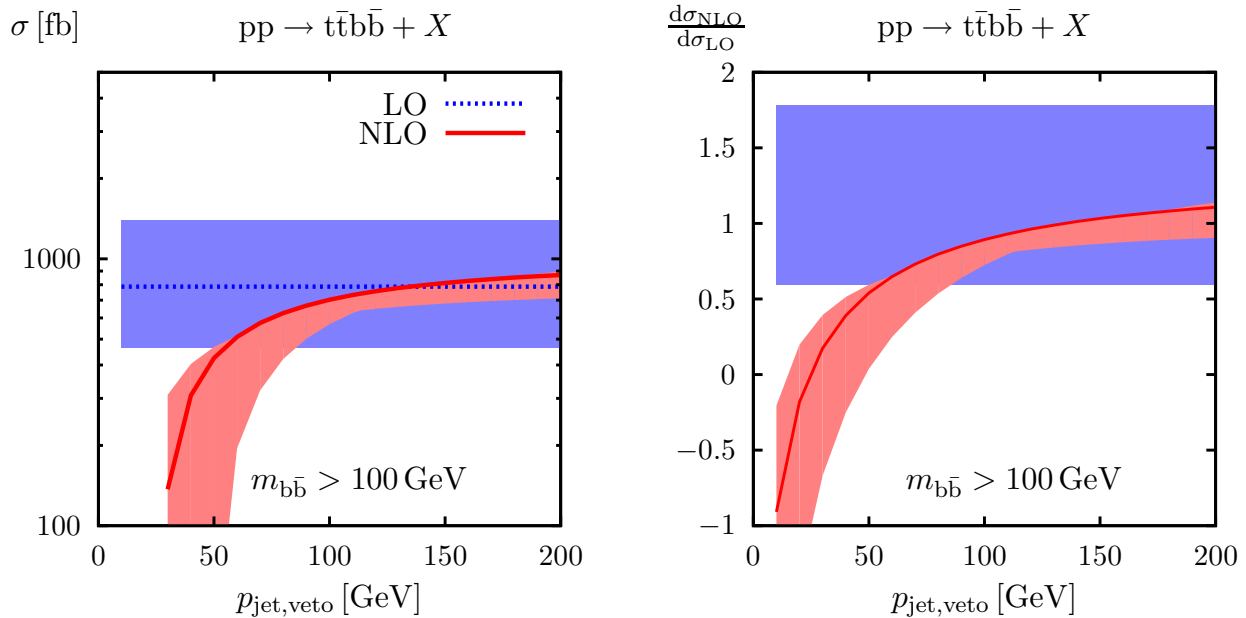


Figure 5: Dependence of the $pp \rightarrow t\bar{t}b\bar{b} + X$ cross section on a jet veto ($p_{T,\text{jet}} < p_{\text{jet,veto}}$) in setup I: absolute LO and NLO predictions (left) and NLO K factor (right). The uncertainty bands correspond to factor-two scale variations.

respect to Ref. [11], where we had a 33% NLO uncertainty, is evident also from the shape of the NLO curves in Figure 4. Now we observe a stable point in the vicinity of the central scale.

Jet veto

As anticipated in Ref. [11], a jet veto can significantly reduce the large cross section of the $t\bar{t}b\bar{b}$ background. This could facilitate the extraction of the $t\bar{t}H$ signal at the LHC. In Figure 5, the integrated $t\bar{t}b\bar{b}$ cross section is plotted versus the upper bound, $p_{\text{jet,veto}}$, imposed to the jet transverse momentum. Here, as well as in the following figures, the left plot shows the absolute LO (blue) and NLO (red) predictions. The curves and their uncertainty bands represent factor-two (uniform) scale variations around the central value (3.2). The right plot displays the LO and NLO bands normalized to the central value of the LO prediction. There the blue band illustrates the relative uncertainty of the LO cross section, i.e. $\sigma_{\text{LO}}(\xi)/\sigma_{\text{LO}}(\xi = 1)$, the red curve corresponds to the K factor, $K = \sigma_{\text{NLO}}(\xi = 1)/\sigma_{\text{LO}}(\xi = 1)$, and the red band shows the variation of the K factor when varying the scales in the NLO cross section but keeping them fixed in the LO cross section, $K_\xi = \sigma_{\text{NLO}}(\xi)/\sigma_{\text{LO}}(\xi = 1)$. In Figure 5 the red (NLO) curve tends to saturate the upper bound of its uncertainty band, a feature that can be observed in various other distributions. This is consistent with the shape of the NLO curve in Figure 4, which develops a maximum in the vicinity of the central scale.

The NLO curve in Figure 5 shows that a sizable reduction of the cross section requires a jet veto well below 200 GeV. For $p_{\text{jet,veto}} = 150, 100,$ and 50 GeV, the K factor is reduced to 1.03, 0.89, and 0.54, respectively. However, there is a trade-off between suppressing the NLO cross section and increasing its perturbative uncertainty. The jet veto tends to

destroy the cancellation between IR logarithms of virtual and real origin and its effect grows as $-\alpha_s^5 \ln^2(E_{\text{thr}}/p_{\text{jet,veto}})$ when $p_{\text{jet,veto}}$ becomes small. Since they are accompanied by an α_s^5 coefficient, these logarithms can give rise to huge scale uncertainties already for moderate values of $p_{\text{jet,veto}}$.

This is reflected by the dramatic amplification of the NLO uncertainty band in Figure 5. Its lower bound enters the pathologic regime of negative cross sections around $p_{\text{jet,veto}} = 50$ GeV. Here, besides the NLO cross section itself, also its uncertainty estimate becomes completely unreliable. The region of small $p_{\text{jet,veto}}$ would require a re-summation. This would stabilize the perturbative calculation and compensate for its divergent behaviour. As a result, the unphysical suppression of the NLO cross section for $p_{\text{jet,veto}} \ll 100$ GeV would be washed out. If we restrict ourselves to the fixed-order NLO result, the plot tells us that jet-veto values around 100 GeV provide a good compromise: the reduction of the K factor is already significant ($K \simeq 0.89$) and the NLO scale uncertainty (19%) is at the same level as for the total cross section (21%).

Invariant-mass distributions

The invariant-mass distribution of the $b\bar{b}$ pair, shown in Figure 6, constitutes a key observable for the search of the $t\bar{t}H$ signal. Because of limited resolution and b-quark combinatorial problems, the Higgs boson would appear as a relatively broad and small peak on top of this distribution. The subtraction of the $t\bar{t}b\bar{b}$ background requires an accurate determination of its normalization, possibly by direct measurement in a signal-free region, and a precise theoretical description of its shape.

In Figure 6 we observe that the NLO predictions perfectly fit within the LO band and significantly reduce the QCD uncertainty over the entire invariant-mass range. The numerical impact of the corrections is moderate and almost constant ($1.21 < K < 1.27$). This favourable behaviour is ensured by the dynamical scale choice (3.2). At high invariant masses the upper bound of the NLO uncertainty band slightly decreases and approaches the central NLO prediction. The same trend appears in the high-energy tail of other distributions.

Figure 7 displays the dependence of the cross section with respect to a cut on the total invariant mass of the $t\bar{t}b\bar{b}$ system ($m_{t\bar{t}b\bar{b}} > m_{\text{cut},t\bar{t}b\bar{b}}$). Since it corresponds to the invariant mass of the $W^+W^-b\bar{b}b\bar{b}$ final state, this quantity is independent of the b-jet combinatorics. It can thus be measured with better resolution as compared to observables that involve only a particular subset of the four b jets. This property might be exploited in order to improve the signal-to-background ratio. Apart from a slight increase in the high invariant-mass tail, the NLO corrections behave similarly as for the $m_{b\bar{b}}$ distribution.

Transverse-momentum distributions

The transverse-momentum distributions of the individual b jets, ordered according to their p_T , are presented in Figure 8 (harder b jet) and Figure 9 (softer b jet). While the softer b jet tends to saturate the lower bound of 20 GeV (3.1), the harder behaves rather differently. Its distribution has a maximum around 100 GeV and a tail that extends up to fairly high transverse momenta. These shapes suggest that one of the two quarks is often emitted from initial-state gluons, while the other one participates to the hard scattering.

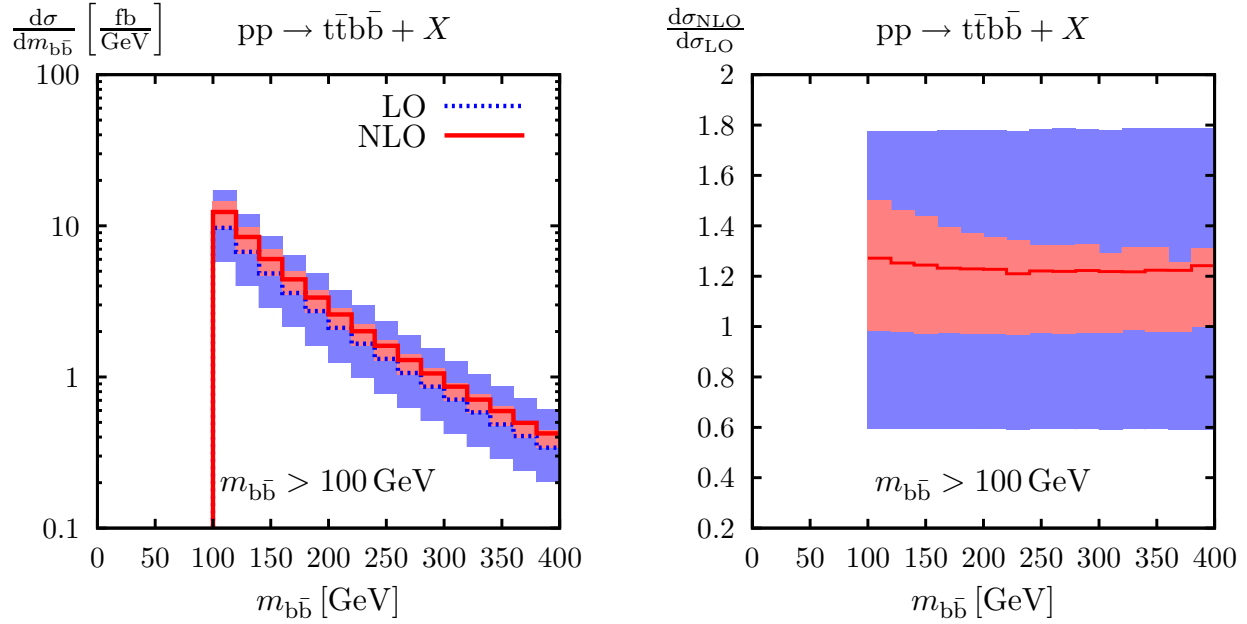


Figure 6: Invariant-mass distribution of the $b\bar{b}$ pair in setup I: absolute LO and NLO predictions (left) and NLO K factor (right). The uncertainty bands correspond to factor-two scale variations.

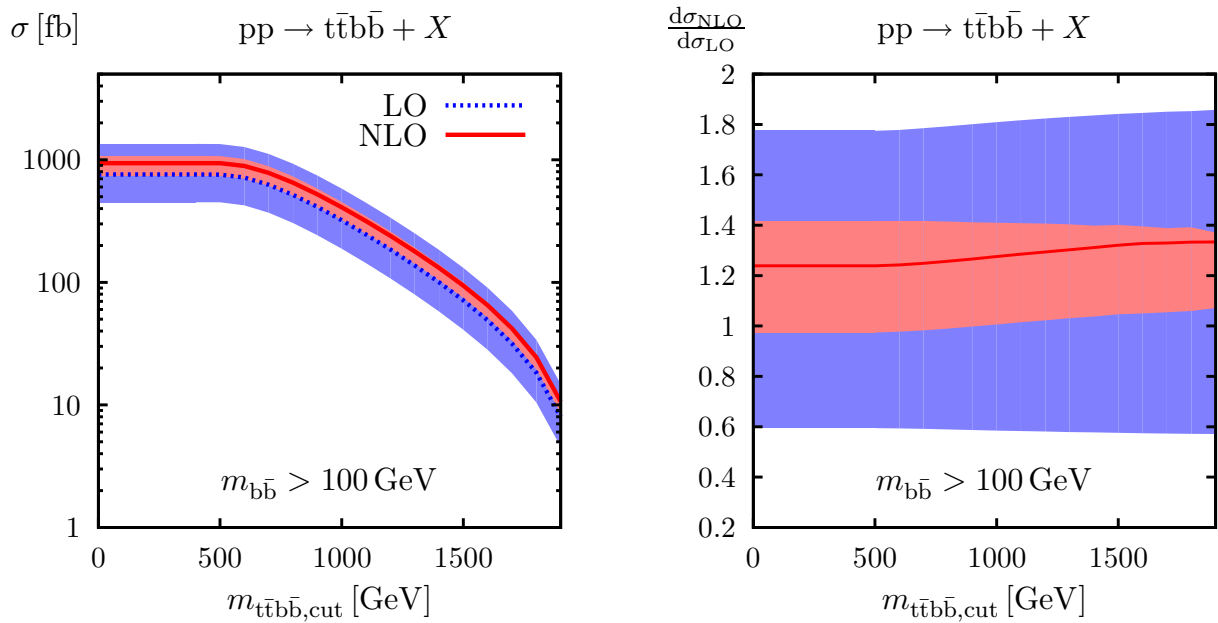


Figure 7: Dependence of the cross section with respect to a cut on the $t\bar{t}b\bar{b}$ invariant mass ($m_{t\bar{t}b\bar{b}} > m_{t\bar{t}b\bar{b},\text{cut}}$) in setup I: absolute LO and NLO predictions (left) and NLO K factor (right). The uncertainty bands correspond to factor-two scale variations.

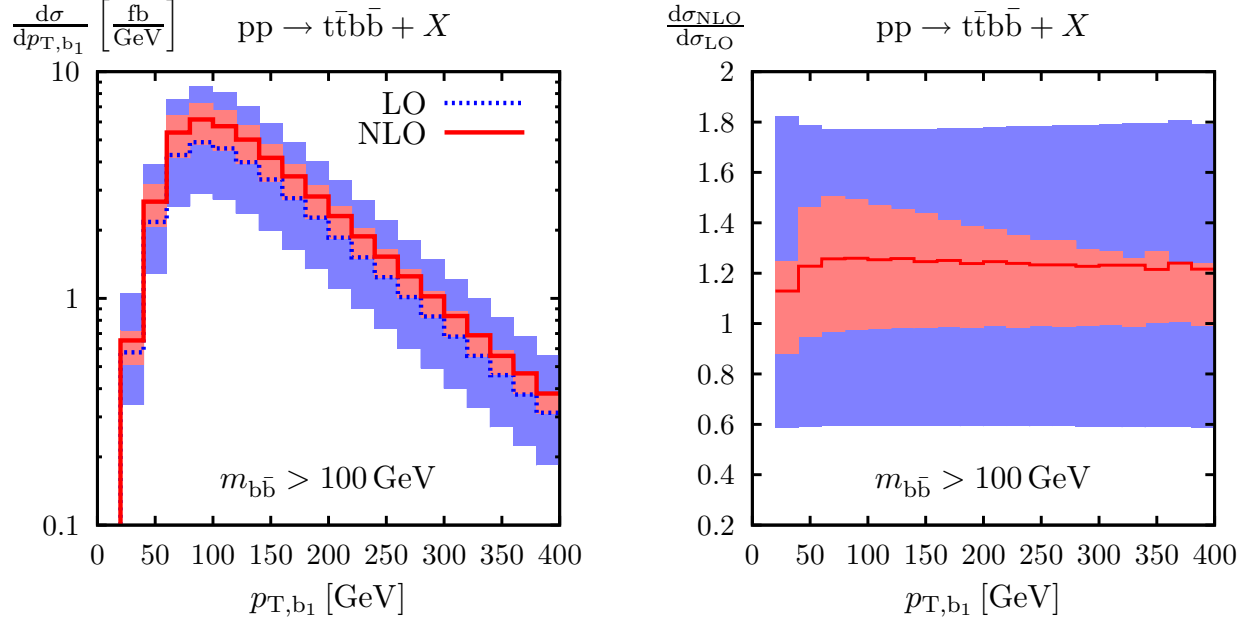


Figure 8: Transverse-momentum distribution of the harder b jet in setup I: absolute LO and NLO predictions (left) and NLO K factor (right). The uncertainty bands correspond to factor-two scale variations.

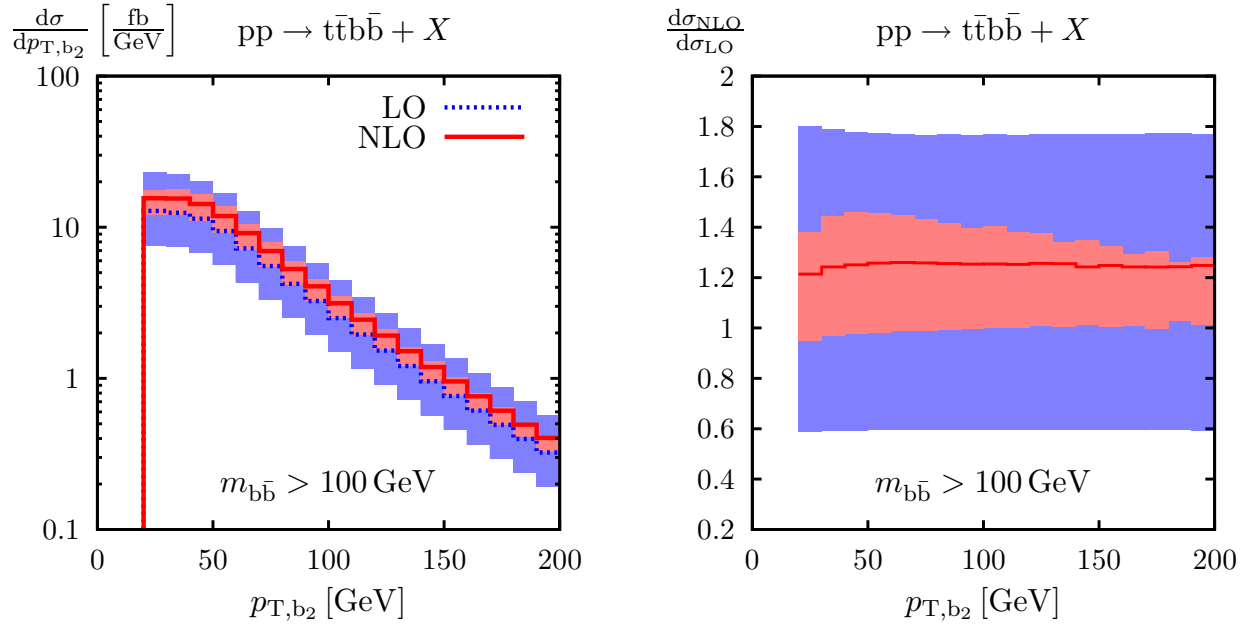


Figure 9: Transverse-momentum distribution of the softer b jet in setup I: absolute LO and NLO predictions (left) and NLO K factor (right). The uncertainty bands correspond to factor-two scale variations.

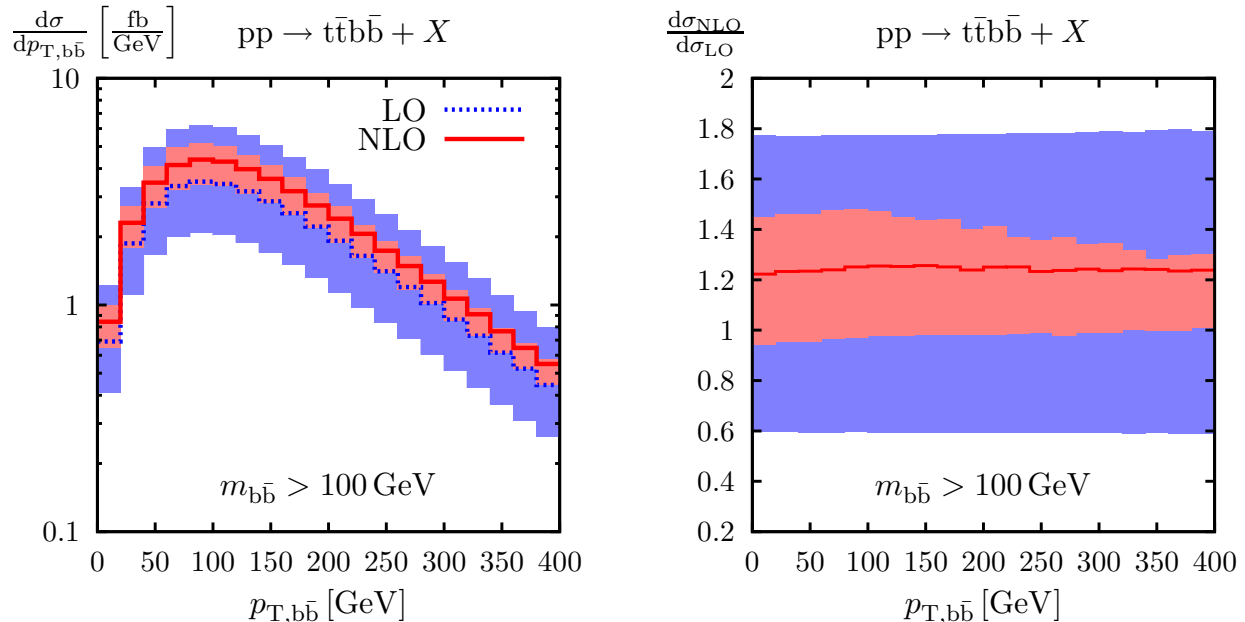


Figure 10: Transverse-momentum distribution of the $b\bar{b}$ system in setup I: absolute LO and NLO predictions (left) and NLO K factor (right). The uncertainty bands correspond to factor-two scale variations.

In contrast, none of the b quarks resulting from $t\bar{t}H$ originates from initial-state radiation. This feature, which renders the cross section quite sensitive to $p_{T,b}$, might be exploited to improve the separation of the $t\bar{t}H$ signal.

The dynamical scale introduced in (3.2) accounts for the different kinematics of the two b jets and the extension of their transverse momenta over a wide p_T range. The goodness of this choice is confirmed by the stability of the K factor over the entire p_T -spectrum. The transverse-momentum distribution of the $b\bar{b}$ pair is shown in Figure 10. Its shape resembles fairly closely that of the harder b -jet distribution. Also the K factor and the scale uncertainties behave similarly.

Rapidity and azimuthal distributions

The rapidities of the individual b jets, ordered in p_T , are shown in Figure 11 (harder b jet) and Figure 12 (softer b jet). Both b jets tend to populate the central region. But this feature is much more pronounced for the harder b jet, while the softer one has a significant probability to be emitted also in the forward and backward directions. The rapidity distribution of the $b\bar{b}$ system (not plotted) resembles that of the harder b jet, and the rapidity-separation distribution (Figure 13) does not suggest any strong correlation between the two b jets. All rapidity distributions receive moderate and almost constant NLO corrections.

The rapidity–azimuthal-angle separation, $\Delta R_{b\bar{b}} = \sqrt{(y_b - y_{\bar{b}})^2 + (\phi_b - \phi_{\bar{b}})^2}$, of the b jets is displayed in Figure 14. The shape of this distribution is determined by three kinematic constraints: the rapidity cut (3.1) is responsible for the suppression at high $\Delta R_{b\bar{b}}$; the sharp lower bound at $\Delta R_{b\bar{b}} = 0.4$ results from the jet algorithm; and the invariant-mass cut $m_{b\bar{b}} > 100 \text{ GeV}$ keeps the two b jets at intermediate ΔR -separations.

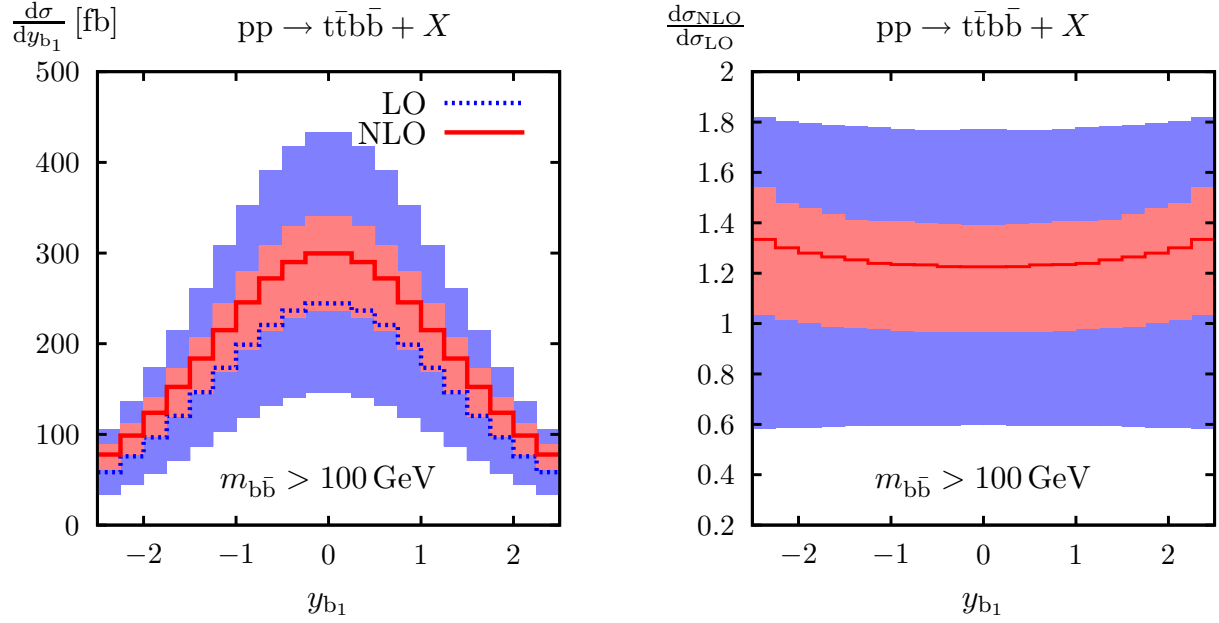


Figure 11: Rapidity distribution of the harder b jet in setup I: absolute LO and NLO predictions (left) and NLO K factor (right). The uncertainty bands correspond to factor-two scale variations.

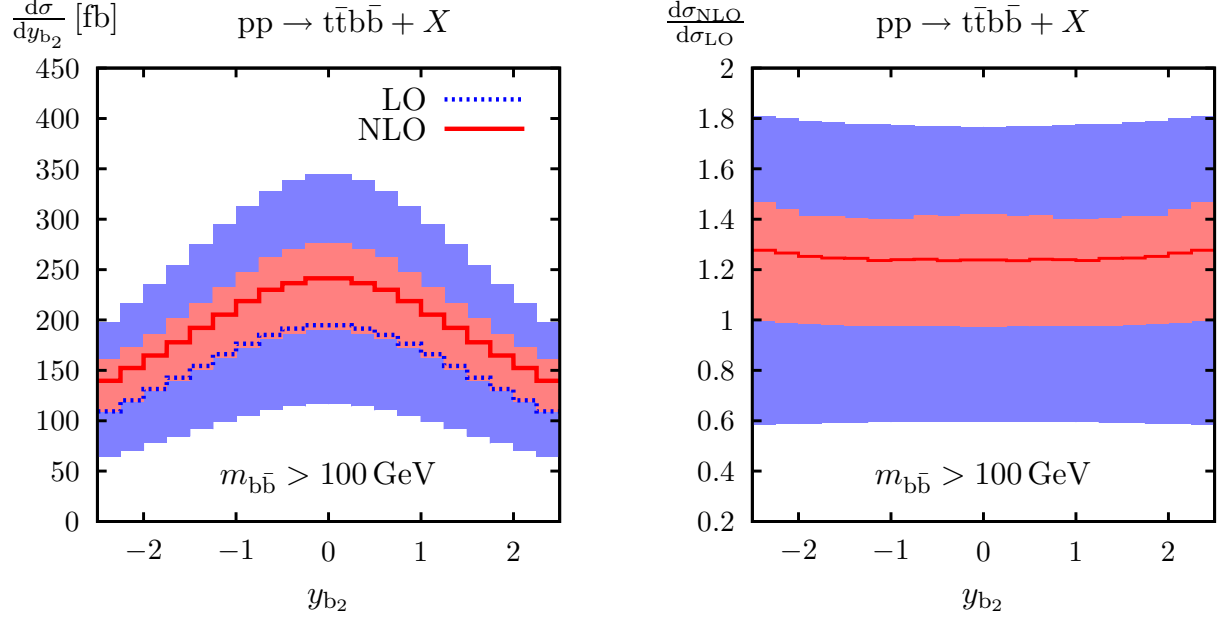


Figure 12: Rapidity distribution of the softer b jet in setup I: absolute LO and NLO predictions (left) and NLO K factor (right). The uncertainty bands correspond to factor-two scale variations.

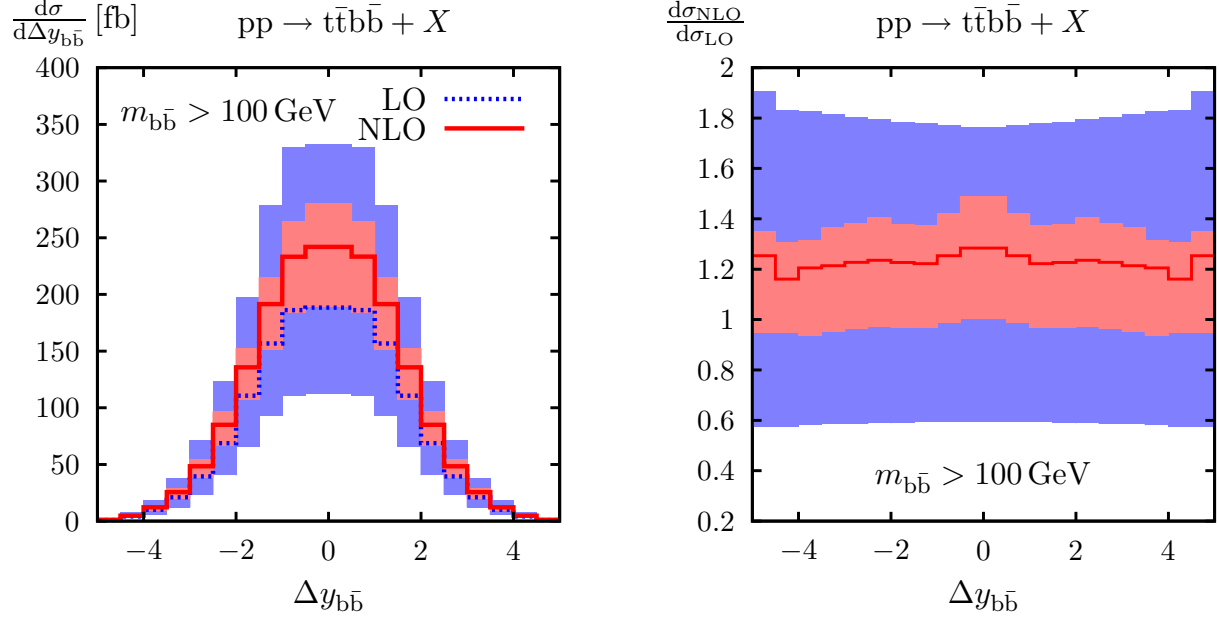


Figure 13: Rapidity separation of the two b jets in setup I: absolute LO and NLO predictions (left) and NLO K factor (right). The uncertainty bands correspond to factor-two scale variations.

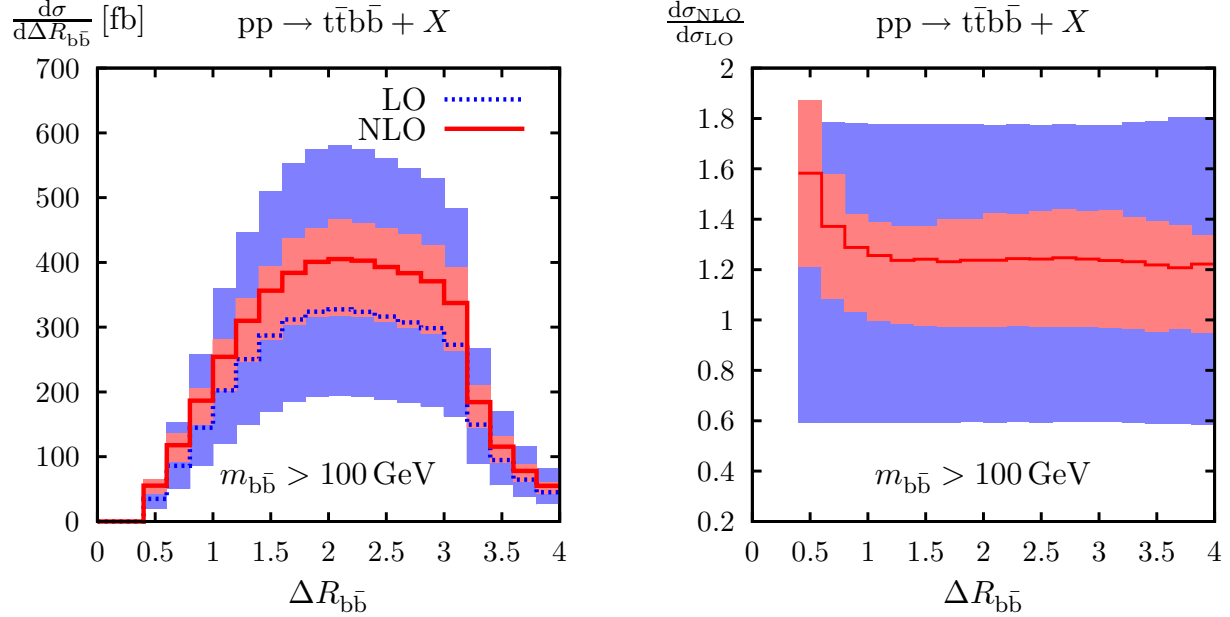


Figure 14: Rapidity-azimuthal-angle separation of the two b jets in setup I: absolute LO and NLO predictions (left) and NLO K factor (right). The uncertainty bands correspond to factor-two scale variations.

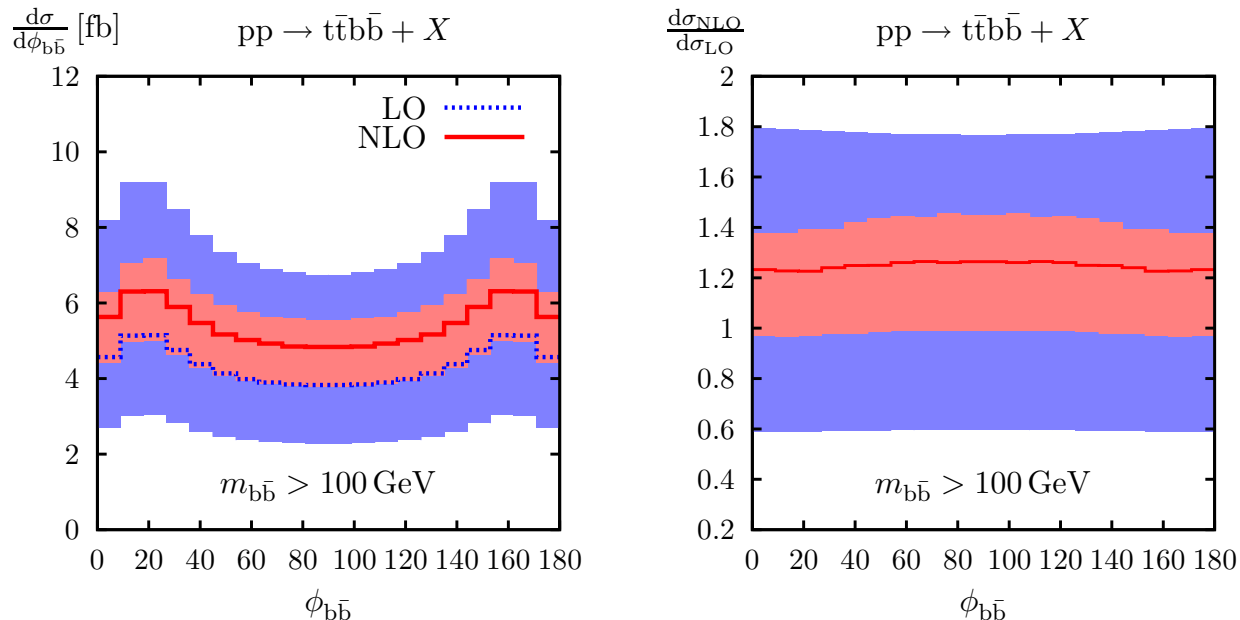


Figure 15: Azimuthal orientation of the b jets in the plane perpendicular to the $b\bar{b}$ system (see text) in setup I: absolute LO and NLO predictions (left) and NLO K factor (right). The uncertainty bands correspond to factor-two scale variations.

The NLO corrections induce a 30–40% distortion of the shape of this distribution in the region $0.4 < \Delta R_{b\bar{b}} \lesssim 1$. This effect can be attributed to the recombination of b quarks and non-b partons, which can turn b-quark pairs with $\Delta R < 0.4$ into b-jet pairs with $\Delta R > 0.4$.

Finally, in Figure 15, we plot the angular variable $\phi_{b\bar{b}}$, which describes the azimuthal orientation of the b jets. This observable is defined as the opening angle between two planes: the “production” plane spanned by the beam axis and the total momentum of the $b\bar{b}$ system, and the “decay” plane, which contains the momenta of the individual b jets, defined by

$$\cos \phi_{b\bar{b}} = \frac{[\mathbf{p}_{\text{beam}} \times (\mathbf{p}_b + \mathbf{p}_{\bar{b}})] \cdot (\mathbf{p}_b \times \mathbf{p}_{\bar{b}})}{|\mathbf{p}_{\text{beam}} \times (\mathbf{p}_b + \mathbf{p}_{\bar{b}})| |\mathbf{p}_b \times \mathbf{p}_{\bar{b}}|}. \quad (3.5)$$

Equivalently $\phi_{b\bar{b}}$ represents the azimuthal orientation of the b jets with respect to the beam direction in the plane perpendicular to the $b\bar{b}$ momentum. In the case where the $b\bar{b}$ pair results from the decay of an intermediate particle, like the Higgs boson in $t\bar{t}H$ production, the spin of the latter can be determined from the $\phi_{b\bar{b}}$ distribution. Since the Higgs boson has spin 0, the $\phi_{b\bar{b}}$ distribution is expected to be isotropic, i.e. $\phi_{b\bar{b}}$ -independent. As we see from Figure 15, the NLO corrections have a negligible influence on the shape of this observable for the $t\bar{t}b\bar{b}$ background.

3.5 Setup II

As discussed in the introduction, the selection of $t\bar{t}b\bar{b}$ signatures with highly boosted b-quark pairs may help to separate the $t\bar{t}H(H \rightarrow b\bar{b})$ signal from its backgrounds. This motivates us to study the irreducible $t\bar{t}b\bar{b}$ background in this particular phase-space

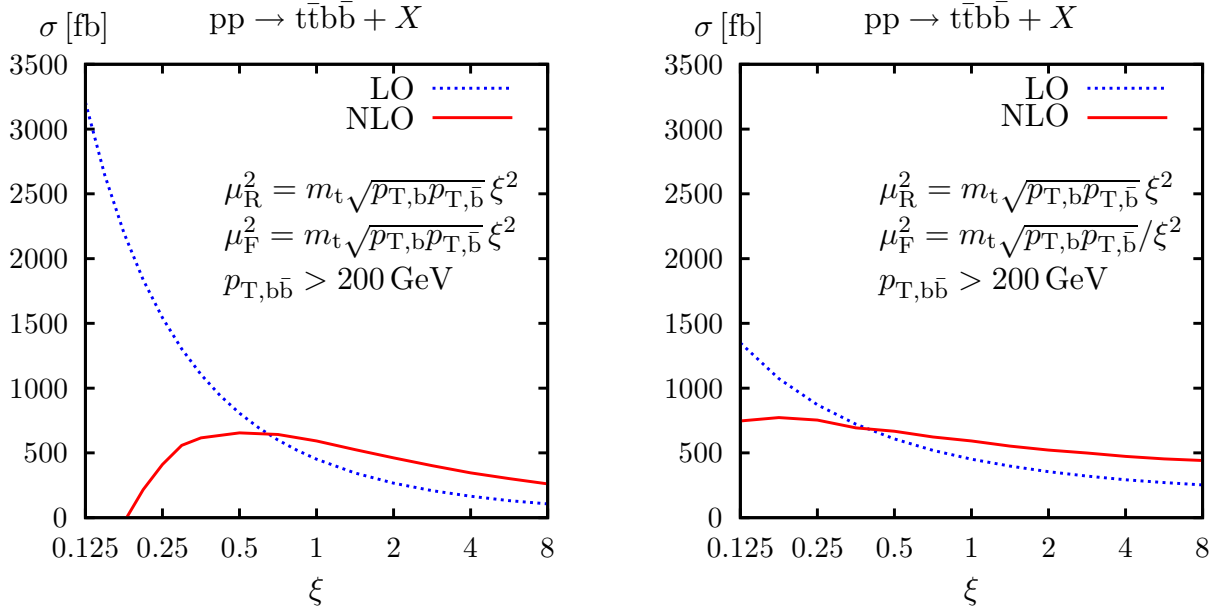


Figure 16: Scale dependence of the LO and NLO $pp \rightarrow t\bar{t}b\bar{b} + X$ cross section at $\sqrt{s} = 14$ TeV in setup II. The left and the right plots describe uniform ($\xi_R = \xi_F = \xi$) and antipodal ($\xi_R = \xi_F^{-1} = \xi$) scale variations, respectively.

region. Specifically, in setup II, we select highly boosted $b\bar{b}$ pairs with $p_{T,b\bar{b}} > 200$ GeV, as proposed in Ref. [9]. In contrast to setup I, here we do not impose any cut on the $b\bar{b}$ invariant mass. Nevertheless the cuts on $p_{T,b\bar{b}}$, $p_{T,b}$, and $p_{T,\bar{b}}$, together with the bound $\Delta R_{b\bar{b}} > 0.4$ resulting from the jet algorithm, impose an effective lower bound

$$m_{b\bar{b}} \simeq \Delta R_{b\bar{b}} p_{T,b\bar{b}} \sqrt{z(1-z)} > \Delta R_{b\bar{b}} p_{T,b,\text{cut}} \sqrt{\frac{p_{T,b\bar{b},\text{cut}}}{p_{T,b,\text{cut}}} - 1} = 24 \text{ GeV}, \quad (3.6)$$

where z and $1-z$ are the (transverse) momentum fractions of the two b jets, and the first equation holds for small $\Delta R_{b\bar{b}}$.

Scale dependence

The scale dependence of the LO and NLO integrated cross sections is shown in Figure 16. At the central scale we obtain $\sigma_{\text{LO}} = 451.8(2)$ fb and $\sigma_{\text{NLO}} = 592(4)$ fb. This corresponds to an NLO correction factor $K = 1.31$. The absolute NLO cross section is reduced by about 40% as compared to setup I. The shape of the scale-dependence curves is quite similar as in Figure 4 and indicates good convergence and stability of the perturbative expansion. The shifts induced by factor-two variations of the QCD scales amount to 79% in LO and 22% in NLO.

Investigating the sensitivity of the NLO cross section to a jet veto we found similar results as in setup I. For a jet veto of 100 GeV the K factor and the NLO uncertainty amount to 0.84 and 33%, respectively.

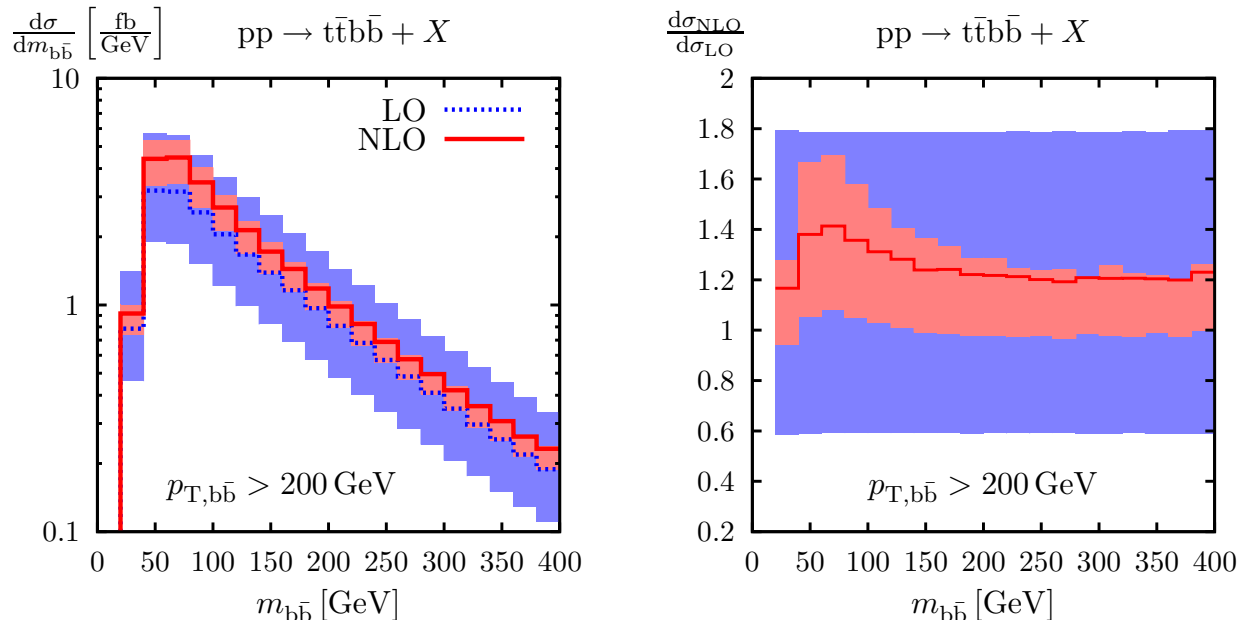


Figure 17: Invariant-mass distribution of the $b\bar{b}$ pair in setup II: absolute LO and NLO predictions (left) and NLO K factor (right). The uncertainty bands correspond to factor-two scale variations.

Invariant-mass and transverse-momentum distributions

The $b\bar{b}$ invariant-mass distribution is displayed in Figure 17. Its behaviour in the region $m_{b\bar{b}} \lesssim 50 \text{ GeV}$ reflects the effective lower bound (3.6). We find that the NLO corrections induce an appreciable shape distortion of about 20%, in particular near the physically interesting region of $m_{b\bar{b}} \sim 100 \text{ GeV}$. Such effect tends to mimic a Higgs signal and should be carefully taken into account in the $t\bar{t}H(H \rightarrow b\bar{b})$ analysis.

The transverse-momentum distributions of the harder and softer b jets are presented in Figure 18 and Figure 19, respectively. As a consequence of the cut imposed on the transverse momentum of the b pair, the harder b jet is pushed to much higher p_T values as compared to setup I. The maximum of its distribution is located around 200 GeV. In contrast, the softer b jet is much less sensitive to the $p_{T,b\bar{b}}$ cut and is predominantly produced in the region $20 \text{ GeV} < p_T < 100 \text{ GeV}$. This different kinematic behaviour of the two b jets might be exploited to separate the $t\bar{t}b\bar{b}$ background from the $t\bar{t}H$ signal, where both b jets are produced by the Higgs boson and should thus have more similar p_T -values. The NLO corrections to both $p_{T,b}$ distributions feature a slight transverse-momentum dependence, with 10% variations of the K factor within the plotted range.

Rapidity and azimuthal distributions

The rapidities of the harder and softer b jets are shown in Figures 20 and 21, respectively. Due to the high p_T of the b-pair system, both b jets tend to be more central as compared to setup I. While the K factor is almost insensitive to the rapidity of the soft b jet, the NLO corrections have a non-negligible influence on the shape of the hard-b-jet distribution for $|y_b| > 1$. The rapidity distribution of the $b\bar{b}$ system (not plotted) behaves similarly to the one of the harder b jet.

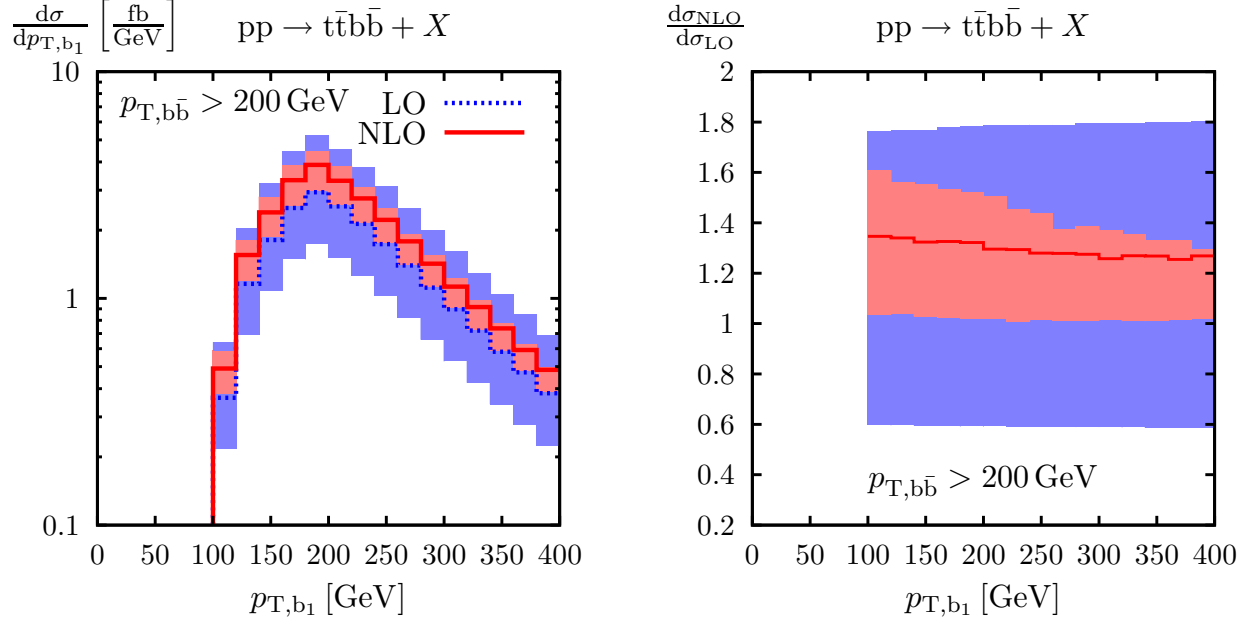


Figure 18: Transverse-momentum distribution of the harder b jet in setup II: absolute LO and NLO predictions (left) and NLO K factor (right). The uncertainty bands correspond to factor-two scale variations.

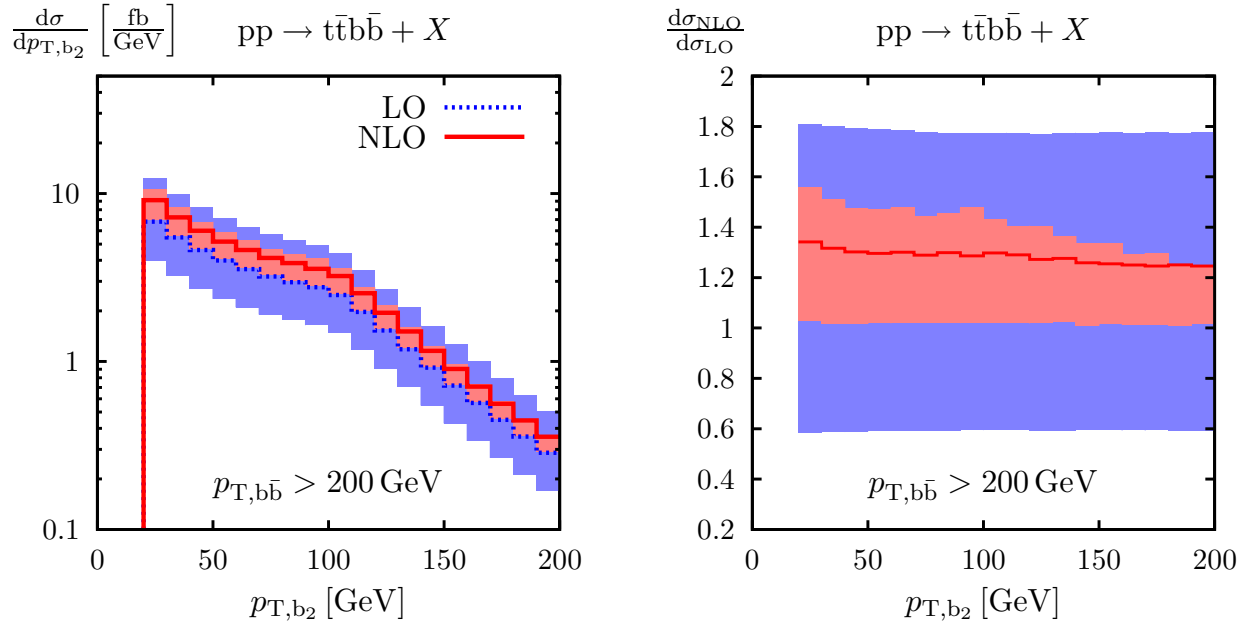


Figure 19: Transverse-momentum distribution of the softer b jet in setup II: absolute LO and NLO predictions (left) and NLO K factor (right). The uncertainty bands correspond to factor-two scale variations.

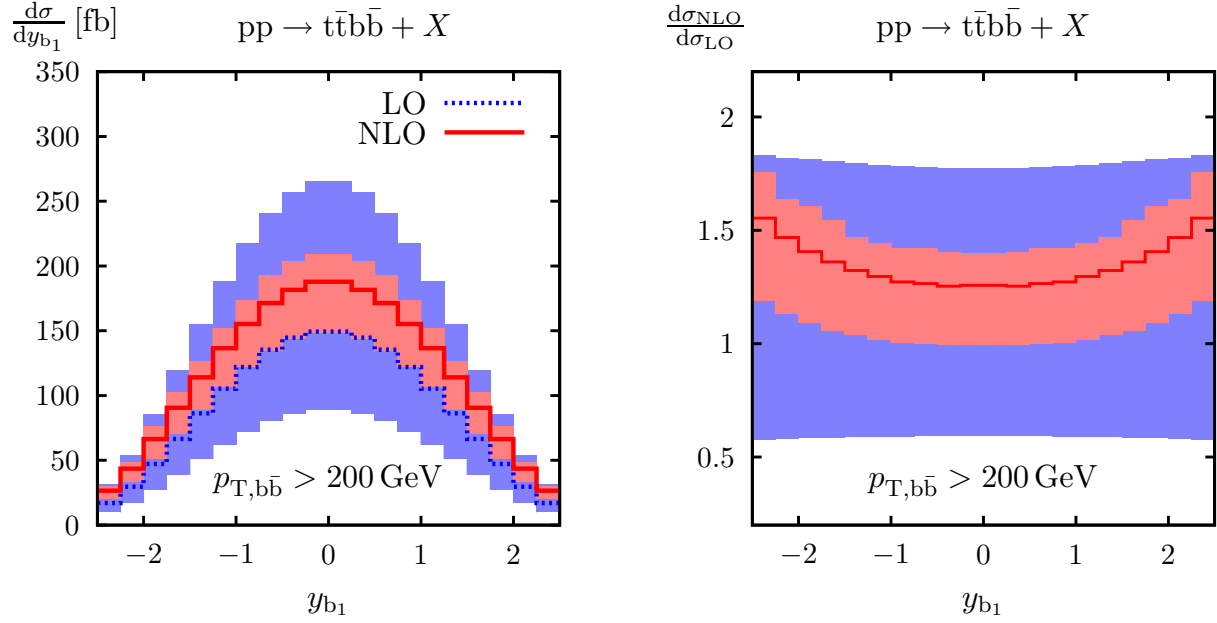


Figure 20: Rapidity distribution of the harder b jet in setup II: absolute LO and NLO predictions (left) and NLO K factor (right). The uncertainty bands correspond to factor-two scale variations.

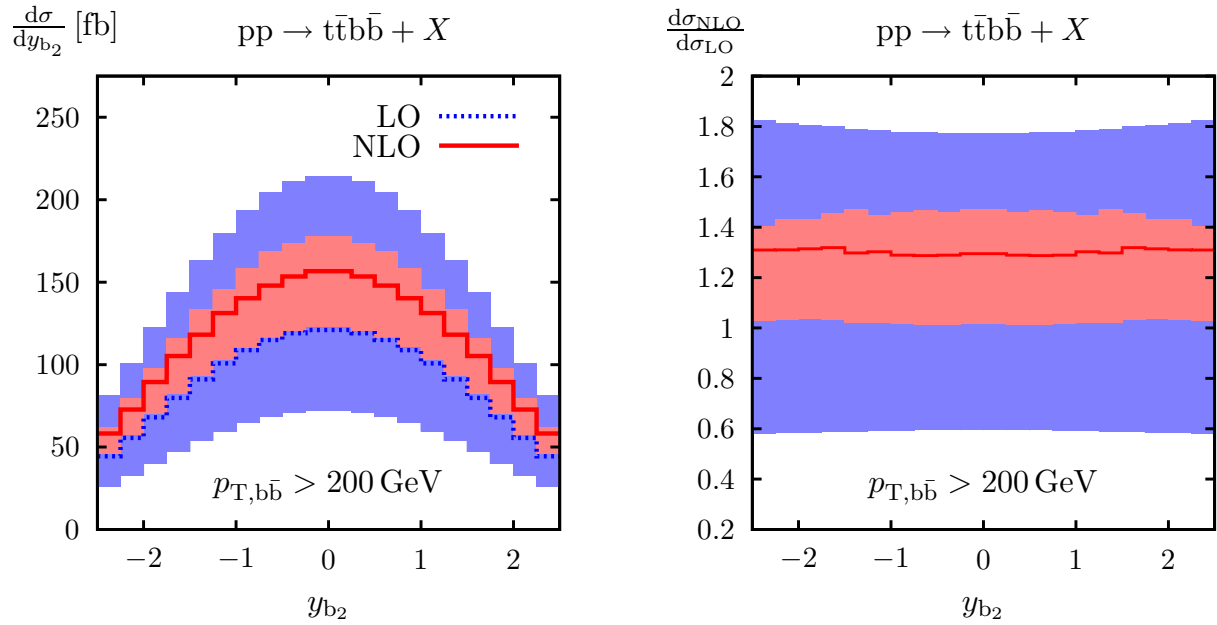


Figure 21: Rapidity distribution of the softer b jet in setup II: absolute LO and NLO predictions (left) and NLO K factor (right). The uncertainty bands correspond to factor-two scale variations.

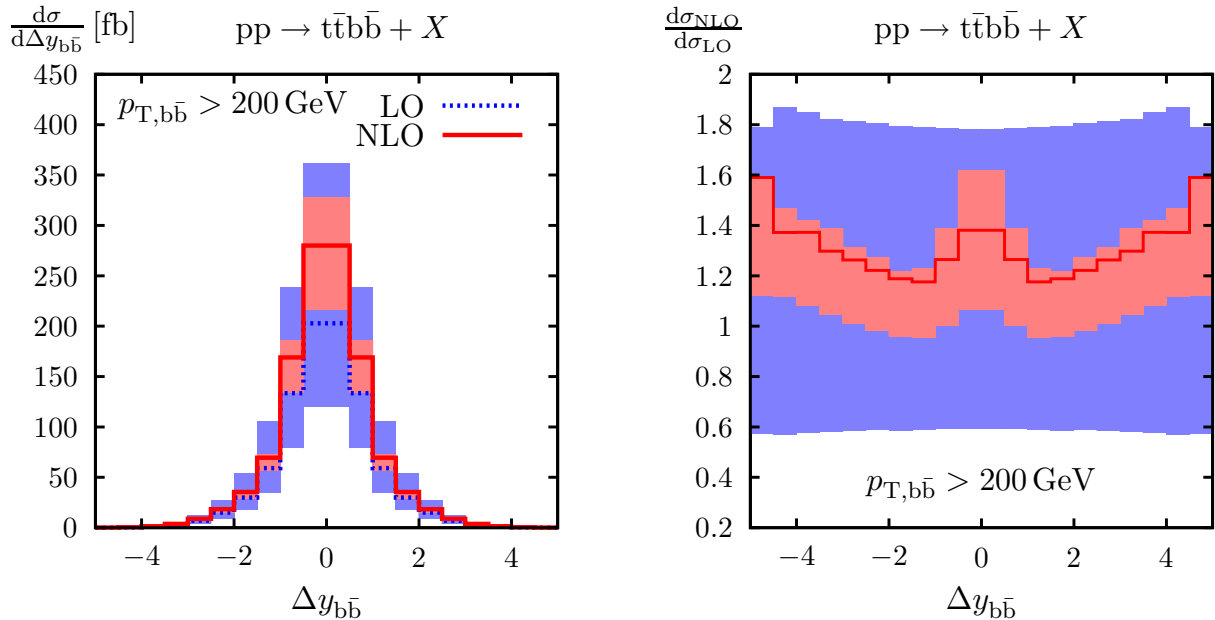


Figure 22: Rapidity separation of the two b jets in setup II: absolute LO and NLO predictions (left) and NLO K factor (right). The uncertainty bands correspond to factor-two scale variations.

The rapidity-separation distribution (Figure 22) is strongly peaked at small $\Delta y_{b\bar{b}}$ and the NLO corrections have an appreciable influence on its shape. In the region $\Delta y_{b\bar{b}} < 2$ the K factor varies between 1.17 and 1.38.

Finally, in Figure 23 we show the rapidity–azimuthal-angle separation of the b jets, which is strongly peaked at small $\Delta R_{b\bar{b}}$. Also in this distribution we observe a significant shape distortion. In the region $\Delta R_{b\bar{b}} < 1$, which corresponds to invariant masses of the order of 100 GeV, the K factor increases by about 20%. This NLO effect might have an important impact on the measurement of $t\bar{t}H$ in the highly-boosted Higgs regime.

3.6 Setup III

In order to explore the effect of a jet veto and its possible correlation with other observables, we have generated events with $m_{b\bar{b}} > 100$ GeV and $p_{T,\text{jet}} < 100$ GeV. The LO and NLO cross sections and their scale dependence are shown in Figure 24. At the central scale we obtain $\sigma_{\text{LO}} = 786.1(6)$ fb and $\sigma_{\text{NLO}} = 700(3)$ fb, corresponding to a correction factor $K = 0.89$. It is evident from Figure 24 that the central scale is very close to a stable point. This demonstrates that a jet-veto value of 100 GeV is sufficiently large to avoid perturbative instabilities. Varying the QCD scales up and down by a factor two shifts the NLO cross section by only 0.4% and -19% , respectively.

Inspecting various kinematic distributions we find that the NLO corrections have a much bigger impact on shapes as compared to setup I. In particular, we observe that the suppression effect resulting from the jet veto is rather sensitive to the transverse momentum of the b jets. For instance, the NLO correction to the p_T distribution of the harder b jet varies by about 15% in the range $20 \text{ GeV} < p_{T,b_1} < 200 \text{ GeV}$.

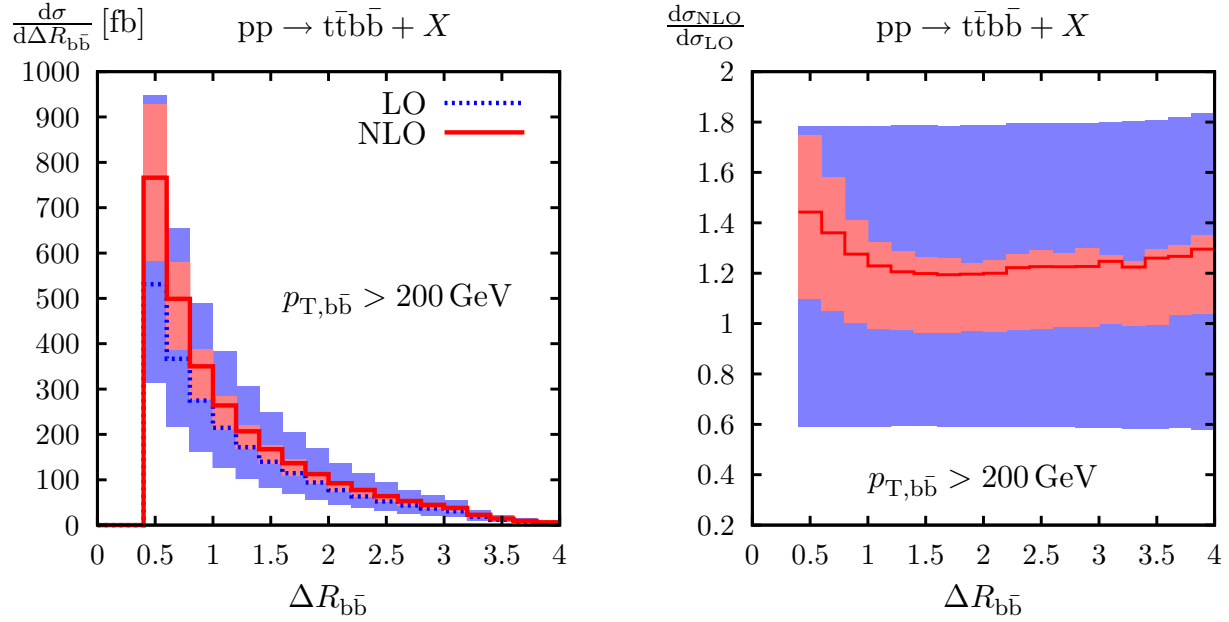


Figure 23: Rapidity-azimuthal separation of the two b jets in setup II: absolute LO and NLO predictions (left) and NLO K factor (right). The uncertainty bands correspond to factor-two scale variations.

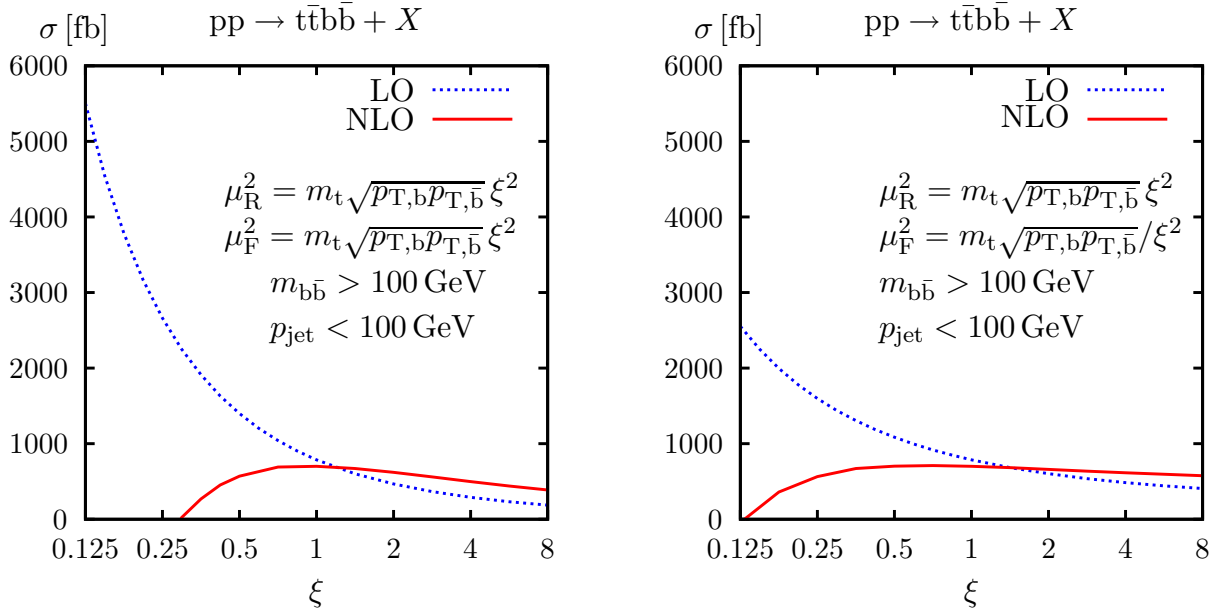


Figure 24: Scale dependence of the LO and NLO $pp \rightarrow t\bar{t}b\bar{b} + X$ cross section at $\sqrt{s} = 14$ TeV in setup III. The left and the right plots describe uniform ($\xi_{\text{R}} = \xi_{\text{F}} = \xi$) and antipodal ($\xi_{\text{R}} = \xi_{\text{F}}^{-1} = \xi$) scale variations, respectively.

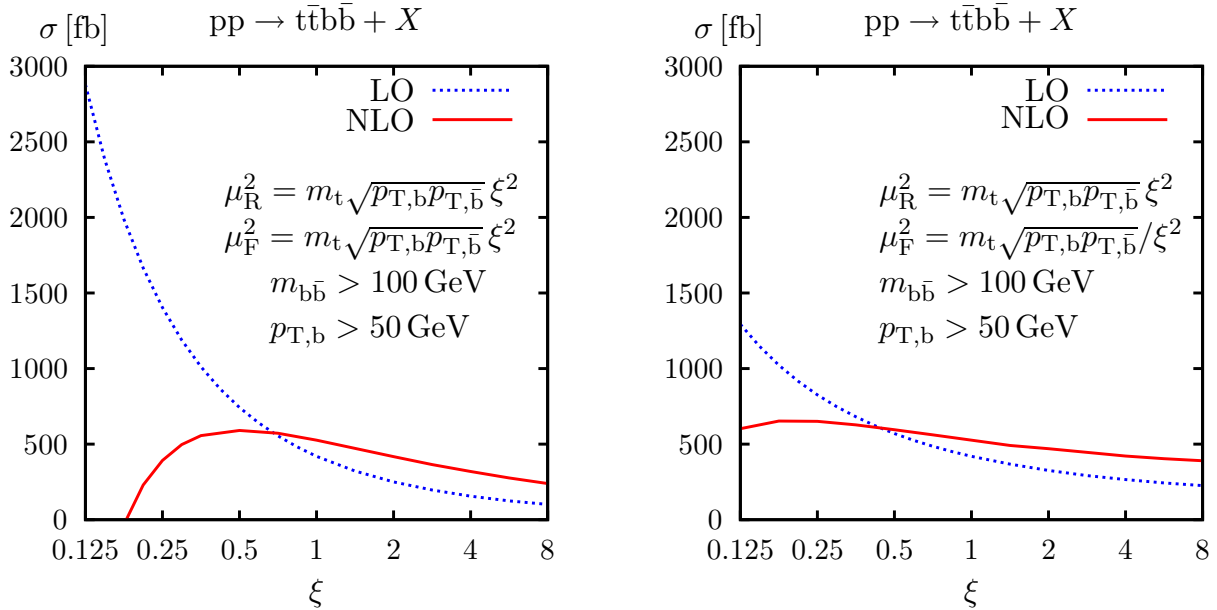


Figure 25: Scale dependence of the LO and NLO $pp \rightarrow t\bar{t}b\bar{b} + X$ cross section at $\sqrt{s} = 14$ TeV in setup IV. The left and the right plots describe uniform ($\xi_R = \xi_F = \xi$) and antipodal ($\xi_R = \xi_F^{-1} = \xi$) scale variations, respectively.

3.7 Setup IV

As observed in Figure 9, the $t\bar{t}b\bar{b}$ cross section is dominated by relatively soft b jets, which tend to saturate the $p_{T,b} > 20$ GeV cut. It is thus interesting to investigate the influence of this cut on the $t\bar{t}b\bar{b}$ background and, in particular, on the NLO corrections. To this end, we have studied a variation of setup I where the $p_{T,b}$ cut is increased from 20 to 50 GeV. The LO and NLO cross sections and their scale dependence are shown in Figure 25. At the central scale we obtain $\sigma_{\text{LO}} = 419.4(1)$ fb and $\sigma_{\text{NLO}} = 526(2)$ fb, corresponding to a correction factor $K = 1.25$. The higher $p_{T,b}$ cut reduces the NLO cross section by 46% as compared to setup I. The LO and the NLO scale dependence remain very similar as in setup I (cf. Figure 4): the uncertainty corresponding to factor-two scale variations amounts to 77% in LO and 21% in NLO.

Inspecting various kinematic distributions we find, as in setup I, that the NLO corrections have little impact on the shapes. In general the kinematic dependence of the NLO correction factor is below 10%. The largest shape distortion is observed in the $\Delta R_{b\bar{b}}$ distribution: similarly as in setup I (cf. Figure 14) we find an increase of the K factor in the region $0.4 < \Delta R_{b\bar{b}} \lesssim 1$ by about 30%.

4 Conclusions

The direct production of $t\bar{t}b\bar{b}$ final states represents the major background to the production of Higgs bosons in association with top–antitop-quark pairs at the LHC, $pp \rightarrow t\bar{t}H$, where the Higgs boson decays into $b\bar{b}$ pairs. This process can lead to a direct measurement of the top-quark Yukawa coupling. Apart from improvements in the experimental analysis, a successful exploitation of this demanding channel requires predic-

tions for $t\bar{t}b\bar{b}$ production at the next-to-leading-order level in QCD, maybe even further improvements.

Extending our first results on the total cross section for $pp \rightarrow t\bar{t}b\bar{b}$ published earlier, we have presented a detailed study of integrated and differential cross sections at the LHC, discussing in particular a dynamical scale choice, the influence of various cuts on the outgoing b quarks, and the impact of a veto on an additional hard jet. We observe that the traditional choice of a constant scale determined by the energy threshold for the process underestimates the $t\bar{t}b\bar{b}$ background by a factor of two, while an appropriate dynamical scale, which is tied to the transverse momenta of the b quarks, stabilizes the perturbative predictions much better. Moreover, the K factor is reduced from 1.8 to 1.2. Using the new scale choice, the corrections have little impact on the shapes of distributions if standard cuts are applied. Strengthening the cut on the transverse momentum of the bottom quarks has no big influence on the K factor and the effect of the NLO corrections on the shape of the distributions. On the other hand, imposing a jet veto of 100 GeV reduces the K factor to 0.9 and enhances the impact of the NLO corrections on the shapes of distributions. In the regime of highly boosted Higgs bosons, which offers better perspectives to observe the $t\bar{t}H$ signal, we find significant distortions of the kinematic distributions, while the K factor is 1.3.

Our calculation builds on the Feynman-diagrammatic approach, i.e. on an algorithmic reduction of each Feynman diagram to a canonical standard form, which is automatically processed to FORTRAN output, and on a numerical reduction of tensor loop integrals to an appropriate set of scalar master integrals. A key feature of the diagram-by-diagram approach is that colour sums can be performed very efficiently. Helicity summation is simplified by introducing a basis of $\mathcal{O}(1000)$ basic structures. The reduction to these structures can be performed in a process-independent way. The numerical tensor-integral reduction employs dedicated methods that have been developed to treat the numerically delicate phase-space regions where small Gram determinants appear in denominators during the traditional tensor reduction. Real corrections are integrated using well-known dipole subtraction methods. We find that our Feynman-diagrammatic approach provides very high numerical stability and CPU efficiency, a result that is very encouraging in view of future challenging next-to-leading-order calculations for important multiparticle processes.

Acknowledgments

We thank Thomas Hahn for technical help in structuring the very long source code, as well as L. Dixon, M. Mangano and C. Papadopoulos for discussions. This work is supported in part by the European Community's Marie-Curie Research Training Network under contract MRTN-CT-2006-035505 "Tools and Precision Calculations for Physics Discoveries at Colliders" and the Japan Society for the Promotion of Science.

Appendix

A Some details on the reduction of standard matrix elements

In Section 2.1 we have briefly described our procedure to reduce the numerous helicity structures for $gg \rightarrow t\bar{t}b\bar{b}$ to a standard form. We proceed in two steps, the first step employing only identities that hold in arbitrary $D \neq 4$ space-time dimensions, followed by the second step (after cancelling UV divergences) that builds on four-dimensional identities. As also anticipated in Section 2.1, we support two different versions of step 2. The first variant only uses the reduction (2.21) of products of five Dirac matrices to products of three or only single matrices, leading to 970 SMEs. In this approach no chiral projectors or γ_5 factors are introduced. The second variant employs more four-dimensional identities, such as (2.20), which are derived from Chisholm's identity in Ref. [10, 66], and leads to 502 SMEs, which however involve the γ_5 matrix.

In the following we describe the second procedure for the crossed process

$$g(p_1) g(p_2) \bar{t}(p_3) t(p_4) \bar{b}(p_5) b(p_6) \rightarrow 0, \quad (\text{A.1})$$

where the incoming momenta of the corresponding incoming particles are given in parentheses. The individual steps to reduce the structures

$$[\bar{v}(p_3)\Gamma_a\omega_\sigma u(p_4)][\bar{v}(p_5)\Gamma_b\omega_\tau u(p_6)] \equiv [\Gamma_a]_{34}^\sigma[\Gamma_b]_{56}^\tau \quad (\text{A.2})$$

are as follows:

1. First, we eliminate multiple contractions of Dirac matrices between the two Dirac chains⁹ by identities like

$$\begin{aligned} \gamma^\mu\gamma^\alpha\gamma^\nu\omega_\pm \otimes \gamma_\mu\gamma^\beta\gamma_\nu &= 4g^{\alpha\beta}\gamma^\mu\omega_\pm \otimes \gamma_\mu\omega_\pm + 4\gamma^\beta\omega_\pm \otimes \gamma^\alpha\omega_\mp, \\ \gamma^\mu\gamma^\alpha\gamma^\nu\omega_\pm \otimes \gamma_\nu\gamma^\beta\gamma_\mu &= 4g^{\alpha\beta}\gamma^\mu\omega_\pm \otimes \gamma_\mu\omega_\mp + 4\gamma^\beta\omega_\pm \otimes \gamma^\alpha\omega_\pm. \end{aligned} \quad (\text{A.3})$$

2. Next we shorten strings of five or more Dirac matrices using (2.21) in the massless bottom-quark chain, $[\bar{v}(p_5)\Gamma_b\omega_\tau u(p_6)]$, leaving three or only one Dirac matrix in this chain. There is at most one contraction of Dirac matrices between the two chains.
3. Now we simplify structures that involve bottom-quark Dirac chains with three slashed vectors using the trick described in (3.40) and (3.41) of Ref. [66]. In more detail, this manipulation replaces the product of two Dirac chains of the form $[\not{d}\not{b}\not{e}\dots]_{34}^\sigma[\not{d}\not{e}\not{f}]_{56}^\tau$ by products in which either the top chain $[\dots]_{34}^\sigma$ has two Dirac matrices less or in which the bottom chain contains only one slashed vector. Using this procedure recursively we obviously achieve that bottom chains with three slashed vectors are multiplied by top chains containing only a single Dirac matrix, i.e. they appear in the form $[\not{d}]_{34}^\sigma[\not{d}\not{e}\not{f}]_{56}^\tau$.

⁹In this context we recall that multiple contractions of Dirac matrices inside a single Dirac chain have already been eliminated in the first (D -dimensional!) step of the algebraic reduction.

4. In a further step it is possible to eliminate all products of three Dirac matrices in the bottom chain, so that this massless Dirac chain contains exactly one Dirac matrix. If there is a contraction between the top and bottom chain, two Dirac matrices can easily be shifted from the bottom to the top chain using (2.20). If there is no contraction the product of chains looks like $[\not{a}]_{34}^\sigma [\not{d}\not{e}\not{f}]_{56}^\tau$ owing to the previous step. If the set $\{d, e, f\}$ contains at most one polarization vector ε_i ($i = 1, 2$) of the two incoming gluons, we can assume that $\{d, e, f\}$ contains either the momentum p_3 or p_4 . If this is not the case, it can be achieved upon using momentum conservation and the Dirac equation in the bottom chain. The factors \not{p}_i ($i = 3, 4$) in the bottom chain easily allow for shifting all but one Dirac matrix to the top chain by the manipulations,

$$\begin{aligned}
[\not{a}]_{34}^\pm [\not{p}_3\not{e}\not{f}]_{56}^\pm &= \frac{1}{2} \left([\gamma_\mu \not{p}_3 \not{a}]_{34}^\pm - m_3 [\gamma_\mu \not{a}]_{34}^\pm \right) [\gamma^\mu \not{e}\not{f}]_{56}^\pm \\
&= \frac{1}{2} \left([\gamma_\mu \not{f}\not{e}\not{p}_3]_{34}^\pm - m_3 [\not{e}\not{f}\gamma_\mu]_{34}^\pm \right) [\gamma^\mu]_{56}^\pm, \\
[\not{a}]_{34}^\pm [\not{p}_3\not{e}\not{f}]_{56}^\mp &= \dots = \frac{1}{2} \left([\not{e}\not{f}\gamma_\mu \not{p}_3]_{34}^\pm - m_3 [\gamma_\mu \not{f}\not{e}]_{34}^\pm \right) [\gamma^\mu]_{56}^\mp, \\
[\not{a}]_{34}^\pm [\not{p}_4\not{e}\not{f}]_{56}^\pm &= \dots = \frac{1}{2} \left([\not{a}\not{p}_4\gamma_\mu \not{f}\not{e}]_{34}^\pm + m_4 [\not{a}\not{e}\not{f}\gamma_\mu]_{34}^\mp \right) [\gamma^\mu]_{56}^\pm, \\
[\not{a}]_{34}^\pm [\not{p}_4\not{e}\not{f}]_{56}^\mp &= \dots = \frac{1}{2} \left([\not{a}\not{p}_4\not{e}\not{f}\gamma_\mu]_{34}^\pm + m_4 [\not{a}\gamma_\mu \not{f}\not{e}]_{34}^\mp \right) [\gamma^\mu]_{56}^\mp, \tag{A.4}
\end{aligned}$$

where we used $p_i^\mu = \{\not{p}_i, \gamma^\mu\}/2$ and the Dirac equation in the 34-chain and (2.20). We recall that we consistently take momenta as incoming. The case that no factor $\not{p}_{3/4}$ appears in the bottom chain can only occur if the other two slashed vectors in the bottom chain belong to polarization vectors. Thus, we can assume that the vector a is a momentum out of $\{p_1, p_2, p_5, p_6\}$ and that $\{d, e, f\}$ contains p_1 or p_2 . We can even omit p_2 on either side if we eliminate it via momentum conservation, so that the considered bottom chains all contain a factor \not{p}_1 . Two Dirac matrices can now be shifted from the bottom to the top chain using the relations

$$\begin{aligned}
[\not{p}_1]_{34}^\pm [\not{p}_1\not{e}\not{f}]_{56}^\pm &= \frac{1}{2} \left([\not{p}_1\gamma_\mu \not{p}_1]_{34}^\pm + p_1^2 [\gamma_\mu]_{34}^\pm \right) [\gamma^\mu \not{e}\not{f}]_{56}^\pm \\
&= \frac{1}{2} \left([\not{p}_1\not{e}\not{f}\gamma_\mu \not{p}_1]_{34}^\pm + p_1^2 [\gamma_\mu \not{e}\not{f}]_{34}^\pm \right) [\gamma^\mu]_{56}^\pm, \\
[\not{p}_1]_{34}^\pm [\not{p}_1\not{e}\not{f}]_{56}^\mp &= \dots = \frac{1}{2} \left([\not{p}_1\gamma_\mu \not{f}\not{e}\not{p}_1]_{34}^\pm + p_1^2 [\not{e}\not{f}\gamma_\mu]_{34}^\pm \right) [\gamma^\mu]_{56}^\mp, \\
[\not{p}_5]_{34}^\pm [\not{p}_1\not{e}\not{f}]_{56}^\pm &= \frac{1}{2} [\gamma_\mu]_{34}^\pm [\gamma^\mu \not{p}_5 \not{p}_1 \not{e}\not{f}]_{56}^\pm = \frac{1}{2} [\gamma_\mu \not{p}_1 \not{p}_5]_{34}^\pm [\gamma^\mu \not{e}\not{f}]_{56}^\pm \\
&= \frac{1}{2} [\gamma_\mu \not{f}\not{e}\not{p}_1 \not{p}_5]_{34}^\pm [\gamma^\mu]_{56}^\pm, \\
[\not{p}_5]_{34}^\pm [\not{p}_1\not{e}\not{f}]_{56}^\mp &= \dots = \frac{1}{2} [\not{p}_5 \not{p}_1 \not{e}\not{f}\gamma_\mu]_{34}^\pm [\gamma^\mu]_{56}^\mp, \\
[\not{p}_6]_{34}^\pm [\not{p}_1\not{e}\not{f}]_{56}^\pm &= \dots = \frac{1}{2} [\not{p}_6 \not{f}\not{e}\not{p}_1\gamma_\mu]_{34}^\pm [\gamma^\mu]_{56}^\pm, \\
[\not{p}_6]_{34}^\pm [\not{p}_1\not{e}\not{f}]_{56}^\mp &= \dots = \frac{1}{2} [\gamma_\mu \not{p}_1 \not{e}\not{f}\not{p}_6]_{34}^\pm [\gamma^\mu]_{56}^\mp, \tag{A.5}
\end{aligned}$$

where we have used that the bottom mass is set to zero, i.e. $m_5 = m_6 = 0$. Note that we did not use $p_1^2 = 0$ in the first relation, in order to indicate that the whole reduction procedure described here does not only apply to gluons but also to the case where gluons are replaced by massive vector bosons.

5. After having reduced all bottom chains to contain only one Dirac matrix we apply (2.21) to the top chain recursively as far as possible. In this way the top chains contain only up to four Dirac matrices.
6. Next we reduce products of the form $[\not{d}\not{b}\not{c}\not{d}]_{34}^\sigma[\not{e}]_{56}^\tau$, which do not involve a contraction. After eliminating p_2 via momentum conservation, the product $\not{d}\not{b}\not{c}\not{d}$ contains one of the factors $\not{p}_1\not{p}_5$, $\not{p}_1\not{p}_6$, or $\not{p}_5\not{p}_6$, because at most two of the slashed vectors can be polarization vectors. The majority of such cases can be reduced with the following relations,

$$\begin{aligned}
[\Gamma\not{d}\not{p}_5]_{34}^\pm[\not{e}]_{56}^\pm &= \frac{1}{2}[\Gamma\not{d}\gamma_\mu]_{34}^\pm[\gamma^\mu\not{p}_5\not{e}]_{56}^\pm = \frac{1}{2}[\Gamma\not{d}\gamma_\mu\not{e}\not{p}_5]_{34}^\pm[\gamma^\mu]_{56}^\pm \\
&= -\frac{1}{2}[\Gamma\not{d}\gamma_\mu\not{p}_5\not{e}]_{34}^\pm[\gamma^\mu]_{56}^\pm + (ep_5)[\Gamma\not{d}\gamma_\mu]_{34}^\pm[\gamma^\mu]_{56}^\pm \\
&= -\frac{1}{2}[\Gamma\gamma_\mu\not{e}]_{34}^\pm[\not{d}\gamma^\mu\not{p}_5]_{56}^\pm + (ep_5)[\Gamma\not{d}\gamma_\mu]_{34}^\pm[\gamma^\mu]_{56}^\pm \\
&= -[\Gamma\not{p}_5\not{e}]_{34}^\pm[\not{d}]_{56}^\pm + (ap_5)[\Gamma\gamma_\mu\not{e}]_{34}^\pm[\gamma^\mu]_{56}^\pm + (ep_5)[\Gamma\not{d}\gamma_\mu]_{34}^\pm[\gamma^\mu]_{56}^\pm \\
&= [\Gamma\not{e}\not{p}_5]_{34}^\pm[\not{d}]_{56}^\pm + (ap_5)[\Gamma\gamma_\mu\not{e}]_{34}^\pm[\gamma^\mu]_{56}^\pm - (ep_5)[\Gamma\gamma_\mu\not{d}]_{34}^\pm[\gamma^\mu]_{56}^\pm, \\
[\Gamma\not{d}\not{p}_5]_{34}^\pm[\not{e}]_{56}^\mp &= \dots = -[\Gamma\not{e}\not{p}_5]_{34}^\pm[\not{d}]_{56}^\mp + (ap_5)[\Gamma\not{e}\gamma_\mu]_{34}^\pm[\gamma^\mu]_{56}^\mp \\
&\quad - (ae)[\Gamma\not{p}_5\gamma_\mu]_{34}^\pm[\gamma^\mu]_{56}^\mp + (ep_5)[\Gamma\not{d}\gamma_\mu]_{34}^\pm[\gamma^\mu]_{56}^\mp, \\
[\Gamma\not{d}\not{p}_6]_{34}^\pm[\not{e}]_{56}^\pm &= \dots = -[\Gamma\not{e}\not{p}_6]_{34}^\pm[\not{d}]_{56}^\pm + (ap_6)[\Gamma\not{e}\gamma_\mu]_{34}^\pm[\gamma^\mu]_{56}^\pm \\
&\quad - (ae)[\Gamma\not{p}_6\gamma_\mu]_{34}^\pm[\gamma^\mu]_{56}^\pm + (ep_6)[\Gamma\not{d}\gamma_\mu]_{34}^\pm[\gamma^\mu]_{56}^\pm, \tag{A.6} \\
[\Gamma\not{d}\not{p}_6]_{34}^\pm[\not{e}]_{56}^\mp &= \dots = [\Gamma\not{e}\not{p}_6]_{34}^\pm[\not{d}]_{56}^\mp + (ap_6)[\Gamma\gamma_\mu\not{e}]_{34}^\pm[\gamma^\mu]_{56}^\mp - (ep_6)[\Gamma\gamma_\mu\not{d}]_{34}^\pm[\gamma^\mu]_{56}^\mp.
\end{aligned}$$

Here Γ is any string of Dirac matrices, and again $m_5 = m_6 = 0$ was used. If $a \neq e$, these relations interchange a and e (if $a = e$ they are useless). Since e can only be p_1 , p_3 , or p_4 , we can use these identities to shift p_3 or p_4 to the top chain, where these momenta are eliminated by the Dirac equation, so that we are left with the cases $e = p_1$. For $[\Gamma\not{p}_5\not{p}_6]_{34}^\sigma[\not{p}_1]_{56}^\tau$ this relation can be used to transfer p_6 to the bottom chain, again triggering the Dirac equation there. We are left with the two cases $[\Gamma\not{p}_1\not{p}_5]_{34}^\sigma[\not{p}_1]_{56}^\tau$ and $[\Gamma\not{p}_1\not{p}_6]_{34}^\sigma[\not{p}_1]_{56}^\tau$, which are reduced according to

$$\begin{aligned}
[\Gamma\not{p}_1\not{p}_6]_{34}^\pm[\not{p}_1]_{56}^\pm &= \frac{1}{2}[\Gamma\not{p}_1\gamma_\mu]_{34}^\pm[\not{p}_1\not{p}_6\gamma^\mu]_{56}^\pm = \frac{1}{2}[\Gamma\not{p}_1\not{p}_6\not{p}_1\gamma_\mu]_{34}^\pm[\gamma^\mu]_{56}^\pm \\
&= (p_1p_6)[\Gamma\not{p}_1\gamma_\mu]_{34}^\pm[\gamma^\mu]_{56}^\pm - \frac{p_1^2}{2}[\Gamma\not{p}_6\gamma_\mu]_{34}^\pm[\gamma^\mu]_{56}^\pm, \\
[\Gamma\not{p}_1\not{p}_5]_{34}^\pm[\not{p}_1]_{56}^\mp &= \dots = (p_1p_5)[\Gamma\not{p}_1\gamma_\mu]_{34}^\pm[\gamma^\mu]_{56}^\mp - \frac{p_1^2}{2}[\Gamma\not{p}_5\gamma_\mu]_{34}^\pm[\gamma^\mu]_{56}^\mp,
\end{aligned}$$

$$\begin{aligned}
[\Gamma \not{a} \not{p}_1 \not{p}_5]_{34}^{\pm} [\not{p}_1]_{56}^{\pm} &= \dots = 2(ap_1) [\Gamma \not{p}_5]_{34}^{\pm} [\not{p}_1]_{56}^{\pm} - 2(ap_5) [\Gamma \not{p}_1]_{34}^{\pm} [\not{p}_1]_{56}^{\pm} \\
&\quad + (p_1 p_5) [\Gamma \not{p}_1 \gamma_{\mu} \not{a}]_{34}^{\pm} [\gamma^{\mu}]_{56}^{\pm} - \frac{p_1^2}{2} [\Gamma \not{p}_5 \gamma_{\mu} \not{a}]_{34}^{\pm} [\gamma^{\mu}]_{56}^{\pm}, \\
[\Gamma \not{a} \not{p}_1 \not{p}_6]_{34}^{\pm} [\not{p}_1]_{56}^{\mp} &= \dots = 2(ap_1) [\Gamma \not{p}_6]_{34}^{\pm} [\not{p}_1]_{56}^{\mp} - 2(ap_6) [\Gamma \not{p}_1]_{34}^{\pm} [\not{p}_1]_{56}^{\mp} \\
&\quad + (p_1 p_6) [\Gamma \not{p}_1 \gamma_{\mu} \not{a}]_{34}^{\pm} [\gamma^{\mu}]_{56}^{\mp} - \frac{p_1^2}{2} [\Gamma \not{p}_6 \gamma_{\mu} \not{a}]_{34}^{\pm} [\gamma^{\mu}]_{56}^{\mp}, \quad (\text{A.7})
\end{aligned}$$

where the Dirac structure Γ and the vector a can be chosen arbitrarily.

7. Now we reduce products of Dirac chains of the type $[\gamma_{\mu} \not{a} \not{p}_1 \not{p}_2]_{34}^{\sigma} [\gamma^{\mu}]_{56}^{\tau}$, i.e. four Dirac matrices in the top chain with a contraction to the bottom chain. Among the vectors a, b, c , there is at least one of the momenta p_1, p_5, p_6 . The momenta p_5, p_6 can be shifted to the bottom chain via (2.20) and subsequently eliminated with the Dirac equation. If only p_1 (but not p_5, p_6) occurs in the top chain, the full Dirac structure can only be $[\gamma_{\mu} \not{p}_1 \not{p}_1 \not{p}_2]_{34}^{\sigma} [\gamma^{\mu}]_{56}^{\tau}$, which is kept as a standard structure.
8. Now we repeat steps 6 and 7 for top chains involving three Dirac matrices, in order to eliminate such structures as far as possible, and subsequently again for top chains with two matrices.
9. The remaining products of the form $[\not{p}_i]_{34}^{\sigma} [\not{p}_j]_{56}^{\tau}$ are reduced as far as possible as described in (B.4) of Ref. [10].
10. Finally, it is convenient to replace all chirality projectors $\omega_{\pm} = (1 \pm \gamma_5)/2$ in terms of vector (no γ_5) and axial-vector ($\propto \gamma_5$) structures in the two Dirac chains, because only the combinations vector \otimes vector and axial-vector \otimes axial-vector contribute owing to the parity symmetry of the process in NLO QCD.

B Benchmark numbers for the virtual corrections

In order to facilitate a comparison to our calculation, in this appendix we provide explicit numbers on the squared LO amplitude and the corresponding virtual correction for a single non-exceptional phase-space point. The set of momenta for the partonic reaction $gg \rightarrow t\bar{t}b\bar{b}$ is chosen as

$$\begin{aligned}
p_g^{\mu} &= (500, 0, 0, 500), \\
p_g^{\mu} &= (500, 0, 0, -500), \\
p_t^{\mu} &= (327.5045589027869, 107.1276753641986, -107.9290580423663, -233.1168284428635), \\
p_{\bar{t}}^{\mu} &= (276.6425142763093, -107.4949148022111, 153.8289259355409, -107.3397668261919), \\
p_b^{\mu} &= (233.9459027189062, 82.55875671042013, -77.70592645955253, 204.6375480757531), \\
p_{\bar{b}}^{\mu} &= (161.9070241019976, -82.19151727240762, 31.80605856637796, 135.8190471933023), \quad (\text{B.1})
\end{aligned}$$

which defines the same phase-space point as already chosen for $q\bar{q} \rightarrow t\bar{t}b\bar{b}$ in Ref. [10]. The components are given in GeV and $m_t = 172.6$ GeV. For the spin- and colour-averaged squared LO amplitude we obtain

$$|\mathcal{M}^{\text{LO}}|^2/g_s^8 = 5.437061775267626 \cdot 10^{-9} \text{ GeV}^{-4},$$

		$\delta^{(2)}$	$\delta^{(1)}$	$\delta^{(0)}$
loops	version 1	-0.1484719139263099	0.0986990876957258	0.4123948722195028
	version 2	-0.1484719139260971	0.0986990876958276	0.4123948722188028
I	version 1	0.1484719139263437	-0.0986990876957289	-0.2125642646365643
	version 2	0.1484719139263439	-0.0986990876957291	-0.2125642646365644
NLO	version 1	0.00000000000000338	-0.0000000000000031	0.1998306075828831
	version 2	0.00000000000002467	0.00000000000000985	0.1998306075822384

Table 3: Various contributions to the virtual NLO corrections to $gg \rightarrow t\bar{t}b\bar{b}$ at the phase-space point (B.1).

$$|\mathcal{M}^{\text{LO}}|^2/g_s^8\Big|_{\text{Madgraph}} = 5.437061775267649 \cdot 10^{-9} \text{ GeV}^{-4}, \quad (\text{B.2})$$

where we divided out the strong coupling constant g_s .

We express NLO contributions in the $2 \rightarrow 4$ phase space as Laurent series in $\epsilon = (4 - D)/2$,

$$|\mathcal{M}|^2 = \left(1 + c_\Gamma \sum_{k=0}^2 \delta_{\text{NLO}}^{(k)} \epsilon^{-k}\right) |\mathcal{M}^{\text{LO}}|^2, \quad (\text{B.3})$$

where we factor out the LO term and the normalization factor

$$\begin{aligned} c_\Gamma &= \frac{(4\pi)^\epsilon \Gamma(1+\epsilon) \Gamma^2(1-\epsilon)}{\Gamma(1-2\epsilon)} = \frac{(4\pi)^\epsilon}{\Gamma(1-\epsilon)} + \mathcal{O}(\epsilon^3) \\ &= (4\pi)^\epsilon \Gamma(1+\epsilon) - \frac{\pi^2}{6} \epsilon^2 + \mathcal{O}(\epsilon^3). \end{aligned} \quad (\text{B.4})$$

We split the result into the two parts,

$$\delta_{\text{NLO}}^{(k)} = \delta_{\text{loops}}^{(k)} + \delta_{\text{I}}^{(k)}, \quad (\text{B.5})$$

which correspond to the contributions of renormalized loop diagrams (loops) and the I operator of the dipole subtraction function as defined in Ref. [53]. The numbers in Table 3 have been obtained in the 't Hooft–Feynman gauge using the 't Hooft–Veltman variant of dimensional regularization (four-dimensional external partons). We set the scale of dimensional regularization and the renormalization scale as $\mu = \mu_R = m_t$. The corresponding values of the strong coupling constant in the renormalization scheme described in Section 3 are

$$\alpha_s(m_t)|_{\text{LO}} = 0.1178730139006150, \quad \alpha_s(m_t)|_{\text{NLO}} = 0.1076396017050965. \quad (\text{B.6})$$

The agreement between our two independent versions of the virtual corrections is typically about 10 digits at regular phase-space points.

Another benchmark result for the virtual corrections to $gg \rightarrow t\bar{t}b\bar{b}$ can be found in Ref. [44]. The quantity presented there and denoted as ‘HELAC-1L’ corresponds to the unrenormalized virtual one-loop correction plus the mass-renormalization contribution (without wave-function and coupling constant renormalization). We find agreement at the 10-digit level.

References

- [1] ATLAS Collaboration, ATLAS Detector and Physics Performance Technical Design Report, Vol. 2, CERN-LHCC-99-15.
- [2] G. Aad *et al.* [The ATLAS Collaboration], arXiv:0901.0512 [hep-ex].
- [3] G. L. Bayatian *et al.* [CMS Collaboration], J. Phys. G **34** (2007) 995.
- [4] B. P. Kersevan and E. Richter-Was, Eur. Phys. J. C **25** (2002) 379 [arXiv:hep-ph/0203148]; Comput. Phys. Commun. **149**, 142 (2003) [arXiv:hep-ph/0201302].
- [5] J. Cammin and M. Schumacher, ATL-PHYS-2003-024.
- [6] V. Drollinger, T. Müller and D. Denegri, arXiv:hep-ph/0111312.
- [7] S. Cucciarelli *et al.*, CMS Note 2006/119; D. Benedetti *et al.*, J. Phys. G **34** (2007) N221.
- [8] J. M. Butterworth, A. R. Davison, M. Rubin and G. P. Salam, Phys. Rev. Lett. **100** (2008) 242001 [arXiv:0802.2470 [hep-ph]].
- [9] T. Plehn, G. P. Salam and M. Spannowsky, arXiv:0910.5472 [hep-ph].
- [10] A. Bredenstein, A. Denner, S. Dittmaier and S. Pozzorini, JHEP **0808** (2008) 108 [arXiv:0807.1248 [hep-ph]].
- [11] A. Bredenstein, A. Denner, S. Dittmaier and S. Pozzorini, Phys. Rev. Lett. **103** (2009) 012002 [arXiv:0905.0110 [hep-ph]].
- [12] G. Bevilacqua, M. Czakon, C. G. Papadopoulos, R. Pittau and M. Worek, JHEP **0909** (2009) 109 [arXiv:0907.4723 [hep-ph]].
- [13] W. Beenakker, S. Dittmaier, M. Krämer, B. Plümper, M. Spira and P. M. Zerwas, Phys. Rev. Lett. **87** (2001) 201805 [arXiv:hep-ph/0107081]; S. Dawson, L. H. Orr, L. Reina and D. Wackerroth, Phys. Rev. D **67** (2003) 071503 [arXiv:hep-ph/0211438]; S. Dawson, C. Jackson, L. H. Orr, L. Reina and D. Wackerroth, Phys. Rev. D **68** (2003) 034022 [arXiv:hep-ph/0305087].
- [14] W. Beenakker, S. Dittmaier, M. Krämer, B. Plümper, M. Spira and P. M. Zerwas, Nucl. Phys. B **653** (2003) 151 [arXiv:hep-ph/0211352].

- [15] S. Dittmaier, P. Uwer and S. Weinzierl, Phys. Rev. Lett. **98** (2007) 262002 [arXiv:hep-ph/0703120] and Eur. Phys. J. C **59** (2009) 625 [arXiv:0810.0452 [hep-ph]].
- [16] A. Lazopoulos, T. McElmurry, K. Melnikov and F. Petriello, Phys. Lett. B **666** (2008) 62 [arXiv:0804.2220 [hep-ph]].
- [17] C. Buttar *et al.* [QCD, EW, and Higgs Working Group], arXiv:hep-ph/0604120.
- [18] Z. Bern *et al.* [NLO Multileg Working Group], arXiv:0803.0494 [hep-ph].
- [19] A. Ferroglia, M. Passera, G. Passarino and S. Uccirati, Nucl. Phys. B **650**, 162 (2003) [arXiv:hep-ph/0209219].
- [20] A. Denner and S. Dittmaier, Nucl. Phys. B **658** (2003) 175 [arXiv:hep-ph/0212259].
- [21] A. Denner and S. Dittmaier, Nucl. Phys. B **734** (2006) 62 [arXiv:hep-ph/0509141].
- [22] F. del Aguila and R. Pittau, JHEP **0407**, 017 (2004) [arXiv:hep-ph/0404120].
- [23] W. T. Giele and E. W. N. Glover, JHEP **0404**, 029 (2004) [arXiv:hep-ph/0402152].
- [24] W. Giele, E. W. N. Glover and G. Zanderighi, Nucl. Phys. Proc. Suppl. **135** (2004) 275 [arXiv:hep-ph/0407016];
R. K. Ellis, W. T. Giele and G. Zanderighi, Phys. Rev. D **73** (2006) 014027 [arXiv:hep-ph/0508308].
- [25] T. Binoth, J. P. Guillet, G. Heinrich, E. Pilon and C. Schubert, JHEP **0510** (2005) 015 [arXiv:hep-ph/0504267].
- [26] T. Binoth, J. P. Guillet and G. Heinrich, JHEP **0702**, 013 (2007) [arXiv:hep-ph/0609054].
- [27] T. Diakonidis, J. Fleischer, J. Gluza, K. Kajda, T. Riemann and J. B. Tausk, Phys. Rev. D **80** (2009) 036003 [arXiv:0812.2134 [hep-ph]].
- [28] T. Diakonidis, J. Fleischer, T. Riemann and J. B. Tausk, Phys. Lett. B **683** (2010) 69 [arXiv:0907.2115 [hep-ph]].
- [29] Z. Bern, L. J. Dixon, D. C. Dunbar and D. A. Kosower, Nucl. Phys. B **435**, 59 (1995) [arXiv:hep-ph/9409265].
- [30] C. F. Berger, Z. Bern, L. J. Dixon, D. Forde and D. A. Kosower, Phys. Rev. D **74**, 036009 (2006) [arXiv:hep-ph/0604195].
- [31] Z. Bern, L. J. Dixon and D. A. Kosower, Annals Phys. **322**, 1587 (2007) [arXiv:0704.2798 [hep-ph]].
- [32] C. F. Berger *et al.*, Phys. Rev. D **78**, 036003 (2008) [arXiv:0803.4180 [hep-ph]].
- [33] R. Britto, F. Cachazo and B. Feng, Nucl. Phys. B **725**, 275 (2005) [arXiv:hep-th/0412103].

- [34] A. Brandhuber, S. McNamara, B. J. Spence and G. Travaglini, *JHEP* **0510**, 011 (2005) [arXiv:hep-th/0506068].
- [35] R. Britto, B. Feng and P. Mastrolia, *Phys. Rev. D* **73**, 105004 (2006) [arXiv:hep-ph/0602178].
- [36] D. Forde, *Phys. Rev. D* **75**, 125019 (2007) [arXiv:0704.1835 [hep-ph]].
- [37] S. D. Badger, E. W. N. Glover and K. Risager, *JHEP* **0707**, 066 (2007) [arXiv:0704.3914 [hep-ph]].
- [38] C. Anastasiou, R. Britto, B. Feng, Z. Kunszt and P. Mastrolia, *JHEP* **0703**, 111 (2007) [arXiv:hep-ph/0612277].
- [39] W. T. Giele, Z. Kunszt and K. Melnikov, *JHEP* **0804**, 049 (2008) [arXiv:0801.2237 [hep-ph]].
- [40] R. K. Ellis, W. T. Giele, Z. Kunszt and K. Melnikov, *Nucl. Phys. B* **822** (2009) 270 [arXiv:0806.3467 [hep-ph]].
- [41] G. Ossola, C. G. Papadopoulos and R. Pittau, *Nucl. Phys. B* **763**, 147 (2007) [arXiv:hep-ph/0609007].
- [42] P. Mastrolia, G. Ossola, C. G. Papadopoulos and R. Pittau, *JHEP* **0806**, 030 (2008) [arXiv:0803.3964 [hep-ph]].
- [43] P. Draggiotis, M. V. Garzelli, C. G. Papadopoulos and R. Pittau, *JHEP* **0904** (2009) 072 [arXiv:0903.0356 [hep-ph]].
- [44] A. van Hameren, C. G. Papadopoulos and R. Pittau, *JHEP* **0909**, 106 (2009) [arXiv:0903.4665 [hep-ph]].
- [45] R. Keith Ellis, K. Melnikov and G. Zanderighi, *Phys. Rev. D* **80**, 094002 (2009) [arXiv:0906.1445 [hep-ph]].
- [46] C. F. Berger *et al.*, *Phys. Rev. D* **80** (2009) 074036 [arXiv:0907.1984 [hep-ph]].
- [47] T. Binoth, N. Greiner, A. Guffanti, J. P. Guillet, T. Reiter and J. Reuter, arXiv:0910.4379 [hep-ph].
- [48] A. Cafarella, C. G. Papadopoulos and M. Worek, *Comput. Phys. Commun.* **180** (2009) 1941 [arXiv:0710.2427 [hep-ph]].
- [49] M. Czakon, C. G. Papadopoulos and M. Worek, *JHEP* **0908** (2009) 085 [arXiv:0905.0883 [hep-ph]].
- [50] S. Catani and M. H. Seymour, *Nucl. Phys. B* **485** (1997) 291 [Erratum-ibid. B **510** (1998) 503] [arXiv:hep-ph/9605323].
- [51] S. Dittmaier, *Nucl. Phys. B* **565** (2000) 69 [arXiv:hep-ph/9904440].

- [52] L. Phaf and S. Weinzierl, JHEP **0104** (2001) 006 [arXiv:hep-ph/0102207].
- [53] S. Catani, S. Dittmaier, M. H. Seymour and Z. Trócsányi, Nucl. Phys. B **627** (2002) 189 [arXiv:hep-ph/0201036].
- [54] F. A. Berends, R. Pittau and R. Kleiss, Nucl. Phys. B **424** (1994) 308 [arXiv:hep-ph/9404313] and Comput. Phys. Commun. **85** (1995) 437 [arXiv:hep-ph/9409326];
F. A. Berends, P. H. Daverveldt and R. Kleiss, Nucl. Phys. B **253** (1985) 441;
J. Hilgart, R. Kleiss and F. Le Diberder, Comput. Phys. Commun. **75** (1993) 191.
- [55] A. Denner, S. Dittmaier, M. Roth and D. Wackerroth, Nucl. Phys. B **560** (1999) 33 [arXiv:hep-ph/9904472] and Comput. Phys. Commun. **153** (2003) 462 [arXiv:hep-ph/0209330].
- [56] S. Dittmaier and M. Roth, Nucl. Phys. B **642** (2002) 307 [arXiv:hep-ph/0206070].
- [57] T. Hahn and M. Pérez-Victoria, Comput. Phys. Commun. **118** (1999) 153 [arXiv:hep-ph/9807565];
T. Hahn, Nucl. Phys. Proc. Suppl. **89** (2000) 231 [arXiv:hep-ph/0005029].
- [58] J. Küblbeck, M. Böhm and A. Denner, Comput. Phys. Commun. **60** (1990) 165;
H. Eck and J. Küblbeck, *Guide to FeynArts 1.0*, University of Würzburg, 1992.
- [59] T. Hahn, Comput. Phys. Commun. **140** (2001) 418 [arXiv:hep-ph/0012260].
- [60] D. B. Melrose, *Nuovo Cimento* **XL A** (1965) 181.
- [61] G. Passarino and M. Veltman, Nucl. Phys. B **160** (1979) 151.
- [62] G. Lei, M. Wen-Gan, H. Liang, Z. Ren-You and J. Yi, Phys. Lett. B **654**, 13 (2007) [arXiv:0708.2951 [hep-ph]].
- [63] G. 't Hooft and M. Veltman, Nucl. Phys. B **153** (1979) 365.
- [64] W. Beenakker and A. Denner, Nucl. Phys. B **338** (1990) 349;
A. Denner, U. Nierste and R. Scharf, Nucl. Phys. B **367** (1991) 637.
- [65] S. Dittmaier, Nucl. Phys. B **675** (2003) 447 [arXiv:hep-ph/0308246].
- [66] A. Denner, S. Dittmaier, M. Roth and L. H. Wieders, Nucl. Phys. B **724** (2005) 247 [arXiv:hep-ph/0505042].
- [67] T. Stelzer and W.F. Long, Comput. Phys. Commun. **81** (1994) 357 [arXiv:hep-ph/9401258];
J. Alwall *et al.*, JHEP **0709** (2007) 028 [arXiv:0706.2334 [hep-ph]].
- [68] S. Dittmaier, Phys. Rev. D **59** (1999) 016007 [arXiv:hep-ph/9805445].
- [69] F. A. Berends and W. T. Giele, Nucl. Phys. B **306**, 759 (1988).

- [70] F. Caravaglios and M. Moretti, Phys. Lett. B **358** (1995) 332 [arXiv:hep-ph/9507237].
- [71] P. Draggiotis, R. H. P. Kleiss and C. G. Papadopoulos, Phys. Lett. B **439**, 157 (1998) [arXiv:hep-ph/9807207].
- [72] R. Frederix, T. Gehrmann and N. Greiner, JHEP **0809** (2008) 122 [arXiv:0808.2128 [hep-ph]].
- [73] A. Bredenstein, S. Dittmaier and M. Roth, Eur. Phys. J. C **44** (2005) 27 [arXiv:hep-ph/0506005].
- [74] M. Ciccolini, A. Denner and S. Dittmaier, Phys. Rev. Lett. **99** (2007) 161803 [arXiv:0707.0381 [hep-ph]] and Phys. Rev. D **77** (2008) 013002 [arXiv:0710.4749 [hep-ph]].
- [75] T. Gleisberg *et al.*, JHEP **0402** (2004) 056 [arXiv:hep-ph/0311263].
- [76] Tevatron Electroweak Working Group and CDF and D0 Collaborations, arXiv:0803.1683 [hep-ex].
- [77] S. Catani, Y. L. Dokshitzer and B. R. Webber, Phys. Lett. B **285** (1992) 291.
- [78] G. C. Blazey *et al.*, arXiv:hep-ex/0005012, in Proceedings of the Physics at RUN II: QCD and Weak Boson Physics Workshop, Batavia, Illinois, 4-6 Nov 1999, p. 47.
- [79] J. Pumplin *et al.*, JHEP **0207** (2002) 012 [arXiv:hep-ph/0201195];
D. Stump *et al.*, JHEP **0310** (2003) 046 [arXiv:hep-ph/0303013].